bioRxiv

Conserved Roles for the Dynein Intermediate Chain and Ndel1 in Assembly and Activation of Dynein

Kyoko Okada[*‡], Bharat R. Iyer[†‡], Lindsay G. Lammers[†], Pedro Gutierrez[*•], Wenzhe Li[*], Steven M. Markus[†#] and Richard J. McKenney[*#]

[*]Department of Molecular and Cellular Biology, University of California, Davis, Davis, CA, USA

[†] Department of Biochemistry and Molecular Biology, Colorado State University, Fort Collins, CO, USA

[•] Present affiliation: Department of Biological Sciences, Columbia University, New York, NY 10027, USA

[#]Correspondence should be addressed to Steven M. Markus (Steven.Markus@colostate.edu) and Richard J. McKenney (rjmckenney@ucdavis.edu)

[‡] Co-first authors

Cytoplasmic dynein, the primary retrograde microtubule transport motor within cells, must be activated for processive motility through the regulated assembly of a dynein-dynactin-adapter (DDA) complex. The interaction between dynein and dynactin was initially ascribed to the N-terminus of the dynein intermediate chain (IC) and a coiled-coil of the dynactin subunit p150^{Glued}. However, cryo-EM structures of DDA complexes have not resolve these regions of the IC and p150^{Glued}, raising questions about the importance of this interaction. The IC N-terminus (ICN) also interacts with the dynein regulators Nde1/Ndel1, which compete with p150^{Glued} for binding to ICN. Using a combination of approaches, we reveal that the ICN plays critical, evolutionarily conserved roles in DDA assembly by interacting with dynactin and Ndel1, the latter of which recruits the DDA assembly factor LIS1 to the dynein complex. In contrast to prior models, we find that LIS1 cannot simultaneously bind to Ndel1 and dynein, indicating that LIS1 must be handed off from Ndel1 to dynein in temporally discrete steps. Whereas exogenous Ndel1 or p150^{Glued} disrupts DDA complex assembly *in vitro*, neither perturbs preassembled DDA complexes, indicating that the IC is stably bound to p150^{Glued} within activated DDA complexes. Our study reveals previously unknown regulatory steps in the dynein activation pathway, and provides a more complete model for how the activities of LIS1/Ndel1 and dynactin/cargo-adapters are integrated to regulate dynein motor activity.

Introduction

Cytoplasmic dynein-1 (hereafter referred to as dynein) transports a wide variety of cellular cargoes toward the minus ends of microtubules. The importance of dynein's cellular functions is highlighted in patients with mutations in the genes that encode dynein or its regulators. Dysregulated dynein function underlies several human neurological diseases, including the malformations in cortical development (MCD) diseases lissencephaly, polymicrogyria, and microcephaly (Alkuraya et al., 2011; Bakircioglu et al., 2011; Fiorillo et al., 2014; Guven et al., 2012; Poirier et al., 2013; Scoto et al., 2015; Willemsen et al., 2012). Although recent biochemical and structural studies have begun to shed light on the molecular basis by which this enormous motor complex is assembled and activated to transport its myriad cellular cargoes (Carter et al., 2016; Markus et al., 2020), numerous questions remain unanswered. Primary among them are the precise roles of the ubiquitous regulators LIS1, and the paralogs Nde1/Ndel1 in the dynein pathway.

Like most molecular motors, dynein assumes an autoinhibited conformation that prevents movement in the absence of cargo (Carter et al., 2016; Markus et al., 2020). The current model for dynein activation posits that the motor must first be released from this state, referred to as the 'phi' particle (due to its resemblance to the Greek character) (Amos, 1989). Upon adopting the uninhibited, but still non-motile, 'open' conformation – with the help of the lissencephaly-related protein LIS1 – it becomes competent for interactions with various cargo-specific adaptor molecules and its activating complex dynactin (Markus et al., 2020; Reck-Peterson et al., 2018). Once assembled, super-processive dynein-dynactin-adaptor (DDA) complexes transport cargos over long distances along microtubules (McKenney et al., 2014; Schlager et al., 2014). Cryo-electron microscopy (cryo-EM) studies have revealed that dynactin serves as a platform that can scaffold as many as two dynein homodimers with their motor domains aligned in a parallel manner that promotes microtubule binding and processive motility (Urnavicius et al., 2018; Zhang et al., 2017).

Cryo-EM studies have also shown, at least in part, how dynein interacts with dynactin. Specifically, the N-terminal 'tail' domains of each dynein heavy chain (HC) dock onto dynactin's mini actin filament (Urnavicius et al., 2015). However, studies that predate identification of these HC-dynactin contacts revealed interactions between the dynein intermediate chain (IC; an accessory subunit of the dynein

complex), and the p150^{Glued} (hereafter p150) subunit of the dynactin complex (Karki and Holzbaur, 1995; Vaughan and Vallee, 1995). Notably, the regions that mediate this interaction are absent from current cryo-EM structures of DDA complexes, raising questions about the physiological importance, and role of the IC-p150 contact in DDA complex assembly.

The absence of these regions from cryo-EM structures is likely due to the flexibility of the relevant portions of IC and p150: the IC N-terminus (ICN), and the C-terminal portion of the first coiled-coil of p150 (p150^{CC1b}) (Karki and Holzbaur, 1995; McKenney et al., 2011; Morgan et al., 2011; Siglin et al., 2013; Tripathy et al., 2014; Vaughan and Vallee, 1995). Within the dynactin complex, p150^{CC1b} is part of an elongated structure that cryo-EM studies have revealed can exist in two possible states: (1) an autoinhibited docked state (minority of particles), in which p150^{CC1} is anchored to the pointed end of the actin filament; and, (2) an undocked state (majority of particles), in which this region is not visible due to its flexibility (Chaaban and Carter, 2022; Lau et al., 2021; Saito et al., 2020; Urnavicius et al., 2015). In contrast to p150^{CC1}, ICN is largely unstructured with a short single alpha helix (SAH) at the very N-terminus that makes direct contacts with p150^{CC1b} (Makokha et al., 2002; McKenney et al., 2011; Morgan et al., 2011), and is also absent from all cryo-EM structures of DDA complexes. Therefore, despite a preponderance of biochemical evidence for interactions between these regions of dynein and dynactin, the field lacks a coherent model for what role(s) these contacts play in the formation of activated DDA complexes.

In addition to p150^{CC1b}, the ICN SAH also interacts with the dynein regulator Nde1 (McKenney et al., 2011; Nyarko et al., 2012). The current model for Nde1 (and its paralog Ndel1) function posits that an ICN-bound Nde1 helps recruit LIS1 to the dynein motor domain (Huang et al., 2012; McKenney et al., 2010; Wang et al., 2013; Zylkiewicz et al., 2011). However, one study reported a direct interaction between Ndel1 and the dynein motor domain (Sasaki et al., 2000), suggesting Nde1/Ndel1 may affect dynein function from two distinct dynein surfaces (the ICN and motor domain). In light of the shared binding region on the ICN for p150^{CC1b} and Ndel1 – which compete for binding (McKenney et al., 2011; Nyarko et al., 2012) – it is unclear at what point in the dynein activation cycle Ndel1 and p150^{CC1b} bind to the ICN, and whether these interactions are required for DDA assembly, stability, or motility.

Here we set out to assess the roles of the ICN and Ndel1 in the function and assembly of dynein and DDA complexes. We performed assays in both budding yeast and mammalian systems to determine the extent of evolutionary conservation of these roles. Using a combination of approaches, we find that although the ICN is dispensable for dynein complex integrity, it is a conserved hub that mediates interactions with both Ndel1 and p150 that are required for the assembly and activity of DDA complexes *in vitro* and *in vivo*. We find that contacts between ICN and p150 are critically important during DDA assembly, and that they likely persist during processive motility. With the help of Alphafold2 (AF2) (Jumper et al., 2021), we identify and validate residue-specific interaction surfaces between ICN, Ndel1 and LIS1, and surprisingly find overlapping binding sites on LIS1 for both Ndel1 and dynein, revealing that LIS1 must dissociate from Ndel1 prior to binding the HC. Our data provide new insight into the assembly and activation of DDA complexes and improve our understanding of Nde1's role in this process.

Results

Deletion of the ICN does not disrupt dynein complex integrity or motor activity

The dynein complex consists of two copies each of the heavy chain (HC, Dyn1 in yeast), the intermediate chain (IC, Pac11 in yeast), the light-intermediate chain (LIC, Dyn3 in yeast), and each of the light chains (LC; LC8, TcTEX, Robl in humans; Dyn2 in yeast). While the LCs are thought to help dimerize the ICs, the LICs are involved in mediating interactions with cargo adapter molecules (Reck-Peterson et al., 2018). However, the role of the ICs is less clear. These molecules consist of a disordered N-terminal region, a LC-binding region, and C-terminal WD repeats, which assemble into a beta-propeller that associates with adjacent HC N-terminal tail domains (Urnavicius et al., 2018; Zhang et al., 2017) (Fig. 1A, B, and S1A). As noted above, the N-terminal regions of the ICs are largely unstructured, but possess one (yeast) or two (human) short alpha helices at the extreme N-termini (Figs. 1B, S1A and B) (Jie et al., 2015, 2017; Loening et al., 2020; Morgan et al., 2011; Morgan et al., 2021). To understand the role of the ICN in dynein function, we generated mutant IC alleles of yeast and human dynein as follows: for yeast dynein, we deleted the N-terminal 43 amino acids of Pac11, the only IC variant in this organism; for human dynein, we removed the N-terminal 70 residues of IC2C (Figs. 1B and S1B), which is the most ubiquitously expressed isoform in humans (Ha et al., 2008; Myers et al., 2007). These regions were selected based on their known contacts with p150 (McKenney et al., 2011; Nyarko et al., 2012; Vaughan and Vallee, 1995). These regions do not include the adjacent sequences required to bind to the LCs (Myers et al., 2007; Rao et al., 2013).

Wild-type (WT) and dynein$^{\Delta ICN}$ complexes were purified from yeast or human cells using affinity chromatography. Size-exclusion chromatography and mass photometry revealed no major differences in the shape or masses between WT and mutant dynein complexes, revealing that the ICN is not critical for dynein complex stability (Fig. 1C - D). Consistently, dynein$^{\Delta ICN}$ complexes were indistinguishable from WT motors when viewed by negative stain electron microscopy (Fig. 1E). To confirm the functionality of the mutant motors, we utilized either single molecule assays for yeast dynein, which moves processively

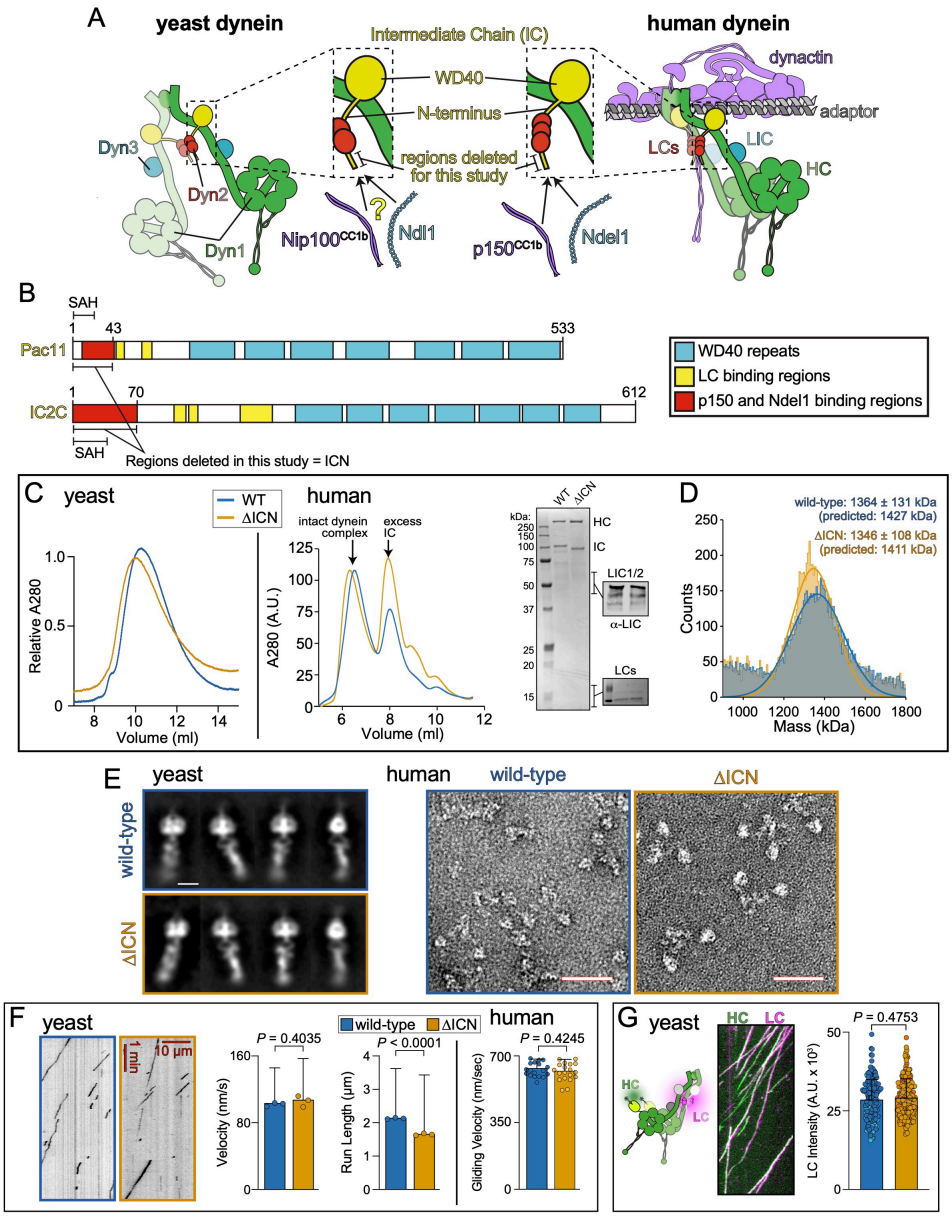

Figure 1. Deletion of the intermediate chain N-terminus has no effect on dynein complex integrity or function. A Cartoon depicting the yeast and metazoan dynein complexes with (right) and without (left) the activating cargo adaptor and dynactin. Inset depicts heavy chain- (HC) and light chain (LC)-bound intermediate chain (IC) with N-terminus (ICN) highlighted. Previous studies suggested that the ICN is an interaction site for both coiled-coil 1b (CC1b) of p150 (Nip100 in yeast) and Ndel1 (Ndl1 in yeast). **B** Schematic of ICs from budding yeast (Pac11) and humans (Dync1l2/IC2C) with domains indicated. SAH, single alpha-helix identified by NMR studies (Morgan et al., 2011).**C** Analytical size exclusion chromatography of wild-type (WT) and dynein$^{\Delta ICN}$ complexes purified from yeast and human cells, along with coomassie-stained gel and immunoblots of human dynein depicting the presence of HC, IC, LIC, and LCs. Data are representative of five independent replicates. **D** Mass photometric analysis of purified human dynein complexes indicate masses correspond to those expected. **E** Negative stain electron micrographs reveal intact dynein complexes from yeast (2D class averages shown; scale bar, 10 nm) and human (raw images shown; scale bars, 50 nm). **F** Representative kymographs, and plots (mean ± SD, along with mean values from individual replicates for single molecule data, with circles representing all data points for gliding velocity; mean value for run length was determined by fitting raw data to one phase decay) depicting motility parameters for purified yeast (using single molecule assays; n = 183/177/174 WT, and 183/177/208 ΔICN motors from 3 independent replicates; *P* values were calculated using a Mann-Whitney test) and human (via microtubule-gliding assays) dynein reveal similar motility parameters between WT and dynein$^{\Delta ICN}$ complexes (n = 20/20 microtubules for either WT or dynein$^{\Delta ICN}$ from 2 replicates; *P* value calculated using two-tailed t-test). **G** Representative kymograph depicting two-color single molecule motility assay in which yeast dynein HC (HaloTag^{JFX49}-Dyn1) and LC (Dyn2-S6^{LD650}) are visualized together. Plot (mean ± SD, along with all data points) depicts fluorescence intensity values for single molecules of Dyn2 bound to either WT or dynein$^{\Delta ICN}$, indicating the mutant binds to the same number of LCs as the WT complex (n = 101/100 and 101/100 Dyn2 foci from WT and dynein$^{\Delta ICN}$ motors, respectively, from 2 independent replicates, represented by different shades of blue and orange). *P* value was calculated using a Mann-Whitney test.

on its own (Reck-Peterson et al., 2006), or multi-motor microtubule gliding assays for human dynein which does not move processively in isolation (McKenney et al., 2014; Schlager et al., 2014; Trokter et al., 2012). Both yeast and mammalian dynein$^{\Delta ICN}$ complexes were motile, confirming the integrity of the mutant dynein motors (Fig. 1F). The only notable difference in motility parameters between WT and dynein$^{\Delta ICN}$ was a modest reduction in run length for the mutant yeast dynein complex. Finally, we confirmed that removal of the ICN did not disrupt binding of the LCs to the IC by SDS-PAGE for human dynein (Fig. 1C), or via dual-color single molecule assays, in which the yeast HC (Dyn1) and LC (Dyn2) were simultaneously visualized (Fig. 1G). For the latter, relative intensity values of fluorescently labeled Dyn2 revealed no significant difference between mutant and WT dynein complexes, indicating a similar degree of LC occupancy for each. We conclude that removal of the IC N-terminus does not disrupt dynein complex stability or activity.

The ICN is critical for dynein function in vivo

We next wondered how deletion of the ICN would affect dynein function in vivo. Dynein plays key roles in mitotic spindle assembly and positioning in many organisms (Echeverri et al., 1996; Gaglio et al., 1996; Heald et al., 1996; Raaijmakers et al., 2013). To examine the role of ICN in vivo, we generated HEK293 cells that inducibly express either WT or IC2C$^{\Delta ICN}$. Immunofluorescence analysis of these cell lines revealed an approximately 3-fold increase in the mitotic index for cells

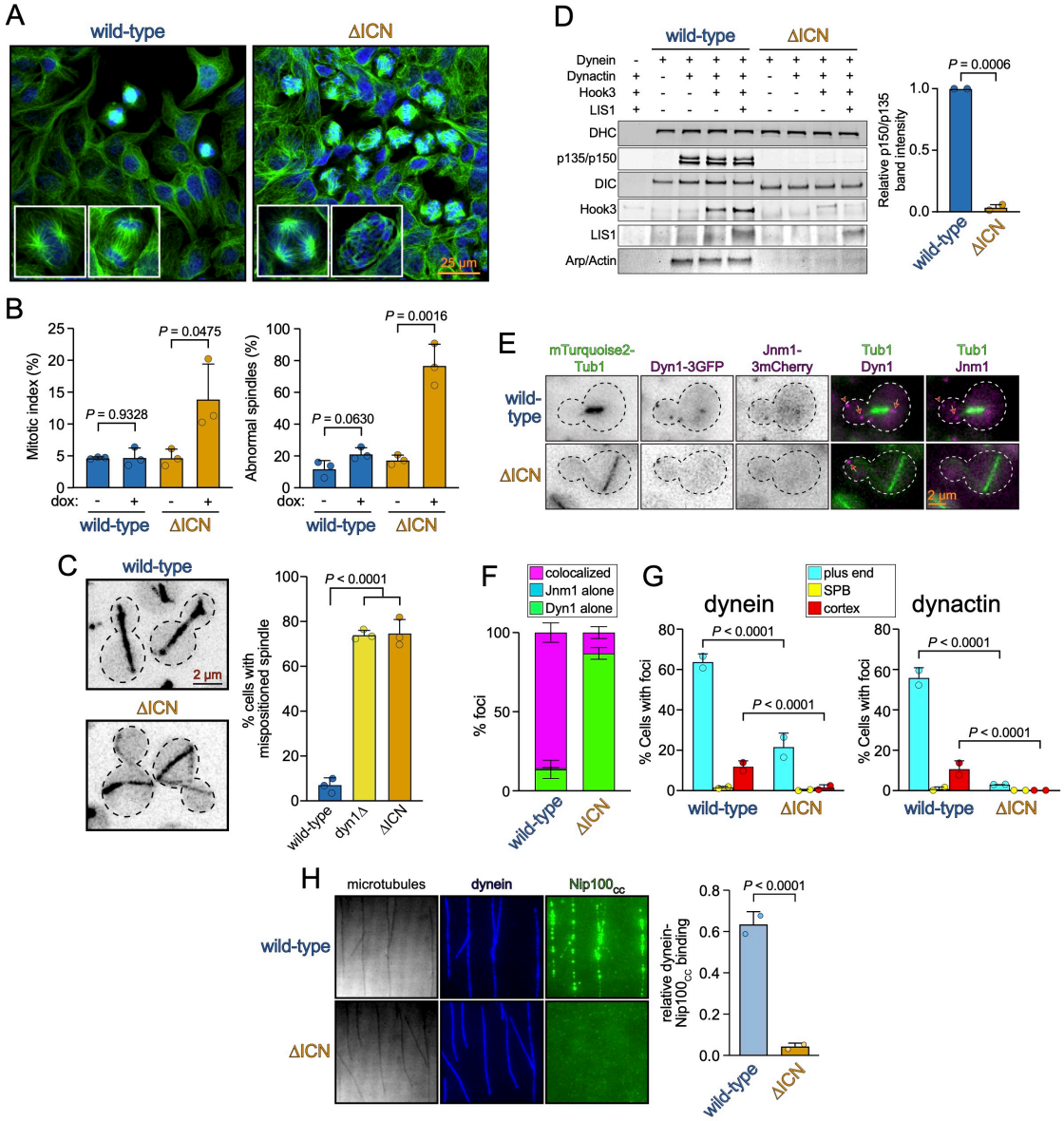

Figure 2. The dynein intermediate chain N-terminus is required for in-cell dynein function and DDA assembly. A Representative fluorescence images of Flp-In™ T-REx™ 293 cells inducibly expressing either WT or IC2C$^{\Delta ICN}$ after being fixed and processed for immunofluorescence. **B** Plots (mean ± SD, along with mean values for individual replicates) depicting fractions of cells in mitosis (mitotic index, left), or those with abnormal spindles (right) for uninduced cells (minus doxycycline), or those induced to express WT or IC2C$^{\Delta ICN}$ (plus doxycycline; n = 717/16/25 uninduced WT cells, 802/50/27 induced WT cells, 1243/29/27 uninduced IC2C$^{\Delta ICN}$ cells, and 1150/45/33 induced IC2C$^{\Delta ICN}$ cells, from 3 independent replicates; *P* values were calculated using two-tailed t-test). **C** Representative inverse fluorescence images of cells expressing fluorescent tubulin (mRuby2-Tub1 for WT and mTurquoise2-Tub1 for dynein$^{\Delta ICN}$), and plot (mean ± SD, along with values from individual replicates) depicting fractions of cells exhibiting mispositioned anaphase spindles (n = 53/56/49 WT cells, 38/56/61 *dyn1Δ* cells, and 49/66/69 *pac11$^{\Delta ICN}$* cells from 3 independent replicates). *P* values were generated by calculating Z score (see Materials and Methods). **D** Immunoblots and plot (mean ± SD, n = 2) depicting relative degree of dynein-dynactin-Hook3 (DDH) assembly as a consequence of mutation (*i.e.*, WT vs ΔICN) or addition of factors (*i.e.*, Hook3, LIS1). *P* value was calculated using a two-tailed t-test. **E** Representative fluorescence images of cells expressing fluorescent tubulin (mTurquoise2-Tub1), Jnm1-3mCherry (homolog of human p50/dynamitin), and either WT or dynein$^{\Delta ICN}$-3GFP (arrows, plus end foci; arrowhead, cortical focus). **F** Plot depicting degree of colocalization for indicated foci in WT or Pac11$^{\Delta ICN}$ cells (mean ± SD; n = 221/193 foci in WT cells, and 57/38 foci in *pac11$^{\Delta ICN}$* cells from 2 independent replicates). **G** Plots (mean ± SD, along with mean values from individual replicates) depicting fractions of cells exhibiting indicated foci (Dyn1-3GFP, dynein; Jnm1-3mCherry, dynactin) at indicated subcellular locale (plus end, SPB, or cortex) in WT or *pac11$^{\Delta ICN}$* cells (Dyn1: n = 266/265 WT cells and 208/200 *pac11$^{\Delta ICN}$* cells from 2 independent replicates; Jnm1: n = 266/265 WT cells and 208/200 *pac11$^{\Delta ICN}$* cells from 2 independent replicates). *P* values were generated from calculating Z scores. **H** Representative images (interference reflection microscopy for microtubules, fluorescence for dynein and Nip100^{CC1}) and quantitation depicting degree to which Nip100^{CC1} binds WT and dynein$^{\Delta ICN}$ (mean ± SD, along with mean values from individual replicates; n = 20 microtubules for each, from 2 independent replicates). *P* value was calculated using an unpaired two-tailed Welch's t-test.

expressing IC2C$^{\Delta ICN}$ compared to those expressing WT IC2C (Fig. 2A and B). Closer inspection revealed that a large fraction of these cells showed aberrant multipolar or disorganized mitotic spindles, a hallmark of dynein dysfunction (Raaijmakers et al., 2013), likely accounting for the increased mitotic index. Thus, the ICN is required for proper spindle assembly and mitotic progression in

mammalian cells, demonstrating a critical role for this domain in dynein function in vivo.

In the budding yeast Saccharomyces cerevisiae, the only known function for dynein and dynactin is to position the mitotic spindle within the bud neck prior to anaphase onset (Carminati and Stearns, 1997; Eshel et al., 1993; Li et al., 1993). Consistent with our observations in mammalian cells, deletion of the Pac11 ICN resulted in a spindle positioning defect as severe as deletion of the dynein heavy chain gene, DYN1, revealing an essential role for ICN in yeast dynein function (Fig. 2C). These observations demonstrate an evolutionarily conserved role for the ICN in dynein functions in mammalian and yeast cells.

Processive dynein motility requires its association with activating cargo adapters and the dynactin complex (McKenney et al., 2014; Schlager et al., 2014). Given the previously identified interaction between ICN and the p150 subunit of dynactin, we wondered whether the ICN plays a role in the association between dynein and dynactin in the context of the activated DDA co-complex. To address this, we combined purified WT or human dynein$^{\Delta ICN}$, mammalian dynactin, and the cargo adapter Hook3 (McKenney et al., 2014), and assayed DDA complex formation via affinity isolation. Consistent with prior results (Baumbach et al., 2017; Duellberg et al., 2014; Jha et al., 2017; Karki and Holzbaur, 1995), we observed an interaction between WT dynein and dynactin in the absence of Hook3, while no dynactin bound to dynein$^{\Delta ICN}$ (Fig. 2D). Addition of Hook3 led to formation of dynein-dynactin-Hook3 (DDH) complexes with WT dynein, but not with dynein$^{\Delta ICN}$ (Fig. 2D). We conclude that the interaction between the ICN and p150 is essential for the assembly of DDA complexes in vitro, and that the inability to form DDA complexes likely underlies the spindle assembly and positioning defects observed in IC2C$^{\Delta ICN}$-expressing human cells, and Pac11$^{\Delta ICN}$-expressing yeast cells.

In budding yeast, pre-assembled dynein-dynactin complexes are delivered to cortical Num1 receptor sites from the plus ends of microtubules. Current data indicate that dynein-Pac1-Bik1 (homologs of human LIS1 and CLIP-170, respectively) complexes first associate with microtubule plus ends, which subsequently recruit dynactin prior to offloading to Num1 (Lee et al., 2003; Markus and Lee, 2011; Markus et al., 2011; Moore et al., 2008; Sheeman et al., 2003). These adaptor-independent dynein-dynactin complexes are likely analogous to those observed above with metazoan proteins (Baumbach et al., 2017; Duellberg et al., 2014; Jha et al., 2017; Karki and Holzbaur, 1995) (Fig. 2D). To assess the role of the ICN in dynein-dynactin binding in yeast, we imaged cells expressing Dyn1-3GFP and Jnm1-3mCherry (homolog of dynactin subunit p50/dynamitin) and quantified the extent of their localization to plus ends, the cell cortex, and spindle pole bodies (SPBs). Whereas WT cells exhibited Dyn1 and Jnm1 foci at all three sites to varying extents (Fig. 2E), the majority of which were colocalized (Fig. 2F), those expressing the Pac11$^{\Delta ICN}$ mutant exhibited very few colocalized foci, indicating that the ICN is required for dynein-dynactin binding at plus ends and the cell cortex. The lack of dynein and dynactin foci at the cell cortex in these cells (Fig. 2G) is consistent with their co-dependence for Num1 binding. However, we also noted a reduction in plus end localization, suggesting that the ICN plays a role in dynein-Pac1 and/or Bik1 binding (see below).

To determine if the ICN of yeast dynein is required for interaction with the p150 homolog in this organism (Nip100), we employed a TIRF microscopy-based assay to measure direct binding between purified yeast dynein and the coiled-coil domain of Nip100. Whereas WT dynein recruited Nip100^{CC1} to microtubules, dynein$^{\Delta ICN}$ complexes did not (Fig. 2H), indicating the ICN indeed mediates the interaction between dynein and Nip100, consistent with prior results using mammalian proteins (McKenney et al., 2011; Nyarko et al., 2012). Taken together, these data indicate that the ICN plays an evolutionarily conserved role in both adaptor-dependent and independent dynein-dynactin binding.

ICN-bound Ndel1 recruits LIS1 to promote dynein localization and activity in cells

In addition to its interaction with p150, previous studies have found that the ICN is also the binding site for Ndel1, which has been implicated in promoting LIS1-dynein binding (Huang et al., 2012; McKenney et al., 2010; Wang et al., 2013; Zylkiewicz et al., 2011). To determine if the ICN of yeast dynein is also required for this interaction, we employed our TIRF microscopy-based assay to measure binding between yeast dynein and Ndl1, the yeast homolog of Ndel1. Whereas WT dynein strongly recruited Ndl1 to microtubules, dynein$^{\Delta ICN}$ complexes did not, indicating the ICN is indeed a conserved hub for binding Ndl1/Ndel1 and p150/Nip100 in yeast and mammals (Fig. 3A) (McKenney et al., 2011; Nyarko et al., 2012). These data also indicate that the ICN is the only contact point on the yeast dynein complex for Ndl1.

Although Ndel1 and Ndl1 have been implicated in recruiting LIS1 and Pac1 to dynein (Huang et al., 2012; Li et al., 2005; McKenney et al., 2010; Wang et al., 2013; Zylkiewicz et al., 2011), the extent to which they do so in cells, and the roles of the ICN in these activities are unclear. Using TIRFM recruitment assays, we found that both yeast and human dynein were able to bind Pac1/LIS1 in the absence of Ndl1/Ndel1. However, increasing concentrations of Ndl1/Ndel1 led to a significant increase in the extent of dynein-Pac1/LIS1 association (Fig. 3B and C; between a 3 and 5-fold increase). In contrast, we observed no such increase for yeast dynein$^{\Delta ICN}$-Pac1 binding, and a greatly attenuated enhancement for human dynein$^{\Delta ICN}$-LIS1 binding (Figs. 3B-C), indicating that ICN-bound Ndl1/Ndel1 is important for the Pac1/LIS1 recruitment to dynein. The extent of the recruitment of Pac1 by Ndl1 was biphasic, with peak recruitment (at 20 nM) followed by a decrease in Pac1 binding at higher Ndl1 concentrations. We noted similar

trends for human dynein$^{\Delta ICN}$, as well as WT human dynein, albeit to lesser extents. We interpret this result as saturation of the microtubule-bound dynein by Ndl1/Ndel1, and subsequent sequestration of Pac1/LIS1 by the excess unbound Ndl1/Ndel1 in solution (see below).

Our data suggest that the role of ICN-bound Ndl1/Ndel1 is to promote dynein-Pac1/LIS1 binding in cells. To validate this model, we assessed the extent of dynein localization in vivo with and without Ndl1. It is well established that the degree of dynein-Pac1 binding in yeast directly correlates with the extent of plus end and cortical association of dynein in cells (Markus and Lee, 2011; Markus et al., 2011). Thus, deletion of Ndl1 would be expected to reduce the extent of dynein targeting to these sites, while its overexpression would increase this localization. Comparison of dynein localization in WT cells versus those lacking Ndl1 (Fig. 3D) (Li et al., 2005) or overexpressing Ndl1 (Fig. 3E) indeed supports this model. These data help explain the reduced localization frequency of dynein$^{\Delta ICN}$ – which cannot bind Ndl1 – in cells (Fig. 2G). Consistent with an important role for Ndl1 in dynein function, a significant fraction of *ndl1Δ* cells exhibit a spindle positioning defect (Fig. S2A). As a more sensitive readout for dynein function, we quantified dynein-mediated spindle movements (Fig. S2B) (Ecklund et al., 2023; Marzo et al., 2019). This revealed that cells lacking Ndl1 indeed possess some dynein activity, albeit to a lesser extent than WT cells. In addition to lower dynein activity metrics (i.e., a reduced extent of dynein-mediated spindle movements, and a lower frequency of such events; Fig. S2E and F), *ndl1Δ* cells exhibit a lower velocity of dynein-mediated spindle movements (Fig. S2C) and a lower 'neck transit' success frequency (Fig. S2G), the latter of which is a read-out for dynein force production (Ecklund et al., 2021; Marzo et al., 2019). These data indicate that dynein does not absolutely rely on Ndl1 for its function (in contrast to Pac1 (Marzo. et al., 2020)), but rather that Ndl1 promotes appropriate localization of dynein to its

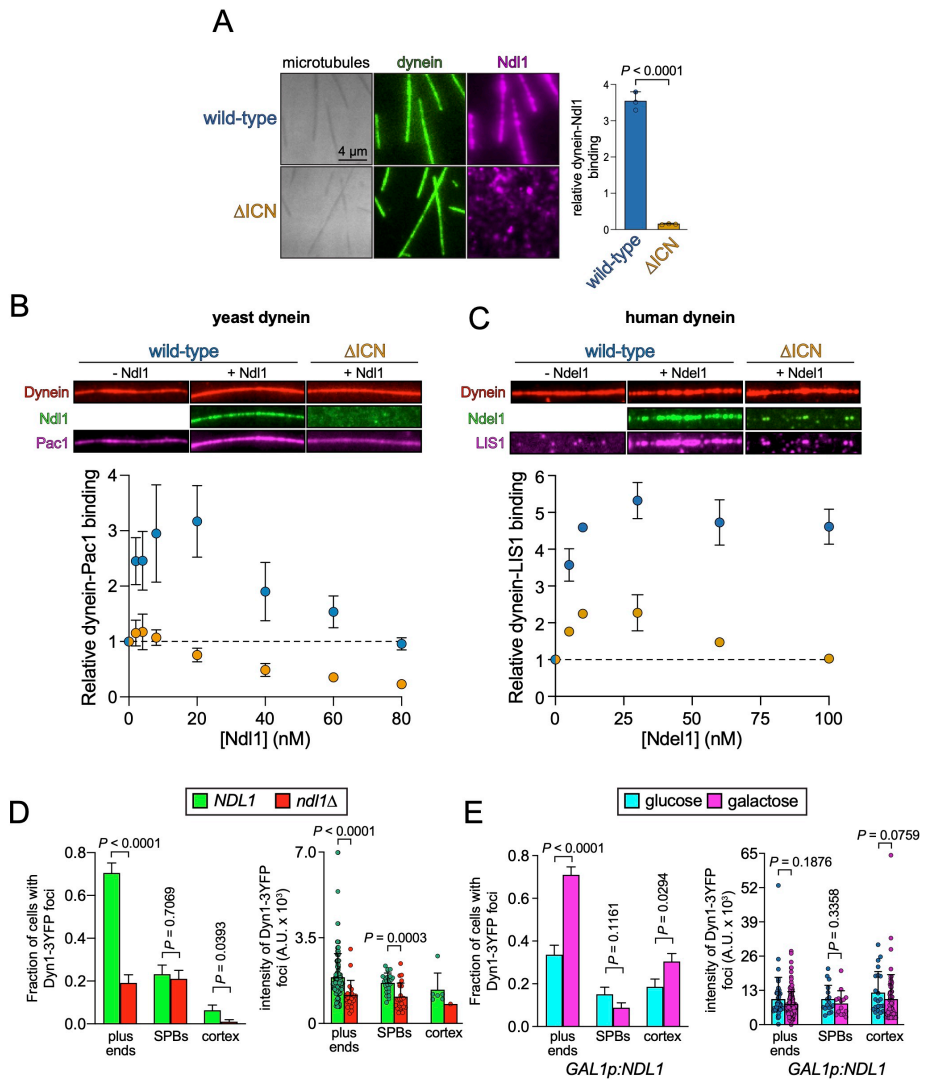

Figure 3. ICN-bound Ndel1/Ndl1 recruits LIS1/Pac1 to promote in-cell dynein localization. A Representative images (interference reflection microscopy for microtubules, fluorescence for dynein and Ndl1) and quantitation (mean ± SD, along with mean values from individual replicates) depicting role of ICN in dynein-Ndl1 binding (n = 30 microtubules for each, from 3 independent replicates). *P* value was calculated using an unpaired two-tailed Welch's t-test. **B and C** Representative fluorescence images and quantitation (mean ± SD; dashed line indicates relative dynein-Pac1/LIS1 binding in the absence of Ndl1/Ndel1) depicting relative dynein-Pac1 **(B)** or LIS1 **(C)** binding. Binding was determined from relative intensity values for microtubule-associated Pac1 or LIS1 with respect to dynein. Note that buffer conditions were used such that neither Pac1, LIS1, Ndl1, nor Ndel1 was recruited to microtubules in the absence of dynein. Thus, the degree of microtubule localization for Pac1, LIS1, Ndl1 and Ndel1 is directly proportional to the extent of their dynein binding **(B:** n = 10/10/10 microtubules for WT, and 10/10/10 microtubules for dynein$^{\Delta ICN}$, from 3 independent replicates; **C:** n = 53/50, 52/45, 56/56, 56/56, 52/72, 56/61 microtubules for WT, and 52/56, 58/53, 51/59, 54/71, 52/52, 55/57 microtubules for dynein$^{\Delta ICN}$, mean ± SD from 2 independent replicates). **D and E** Plots (mean ± SD, as well as all data points for intensity values) depicting the extent of dynein localization (i.e., Dyn1-3GFP) in cells with and without Ndl1 (**D**: n = 95 NDL1 and 105 ndl1Δ cells, and 119 and 48 foci from NDL1 and ndl1Δ cells, respectively, all from 2 independent replicates), or with and without overexpressed Ndl1 (**E**: n = 113 uninduced, and 148 induced cells, and 82 and 245 foci from uninduced and induced cells, respectively, all from 2 independent replicates). P values were calculated using a Mann-Whitney test, or by calculating Z scores. For cells in panel **E**, which were engineered to possess a *GAL1* promoter upstream of the *NDL1* locus, Ndl1 overexpression was controlled by the exclusion or inclusion of galactose in the media for 3 hours immediately prior to imaging.

various subcellular locales by recruiting Pac1 to dynein, thereby enhancing its activity.

Prediction and validation of a Ndel1-LIS1-ICN structure

Although it is well established that Ndel1 and Ndl1 can simultaneously bind LIS1/Pac1 and the ICN (Fig. 3B and C) (Wang and Zheng, 2011; Zylkiewicz et al., 2011) structural information of this complex is lacking. We thus used AlphaFold2-Multimer (using Colabfold) (Jumper et al., 2021; Mirdita et al., 2022) to generate models of the dimeric yeast and human versions of these complexes. The resulting AlphaFold2-Multimer (AF2) models for the human and yeast complexes (Fig. S3A and B) are strikingly similar in their overall appearance, and in the relative positions of the predicted binding sites on Ndel1/Ndl1 for the ICNs, LIS1 and Pac1. Whereas the majority of both Ndel1/Ndl1 proteins are comprised of coiled-coils, the C-termini of both are predicted to be unstructured (Fig. S3A and B). LIS1 and Pac1 are predicted to engage with Ndel1/Ndl1 using both of their WD40 beta-propeller domains, while short alpha-helices within the ICNs are predicted to make contacts with non-overlapping regions near the N-termini of Ndel1/Ndl1 (Fig. S3A, B, 4A and B). Close inspection of the human Ndel1-LIS1-ICN model revealed contact points that have been previously validated. In particular, Ndel1 E119 and R130 (Fig. 4A) have been shown to be important for LIS1 binding (Derewenda et al., 2007), while a group of glutamates at the N-terminus of Ndel1 are required for dynein binding (Fig. S3A) (Wang and Zheng, 2011). NMR studies have also demonstrated the presence of a single alpha-helix (SAH) within the ICN that is required for Ndel1 binding (Nyarko et al., 2012). Based on these experimental validations, we conclude that the AF2 models for the human Ndel1-ICN-LIS1

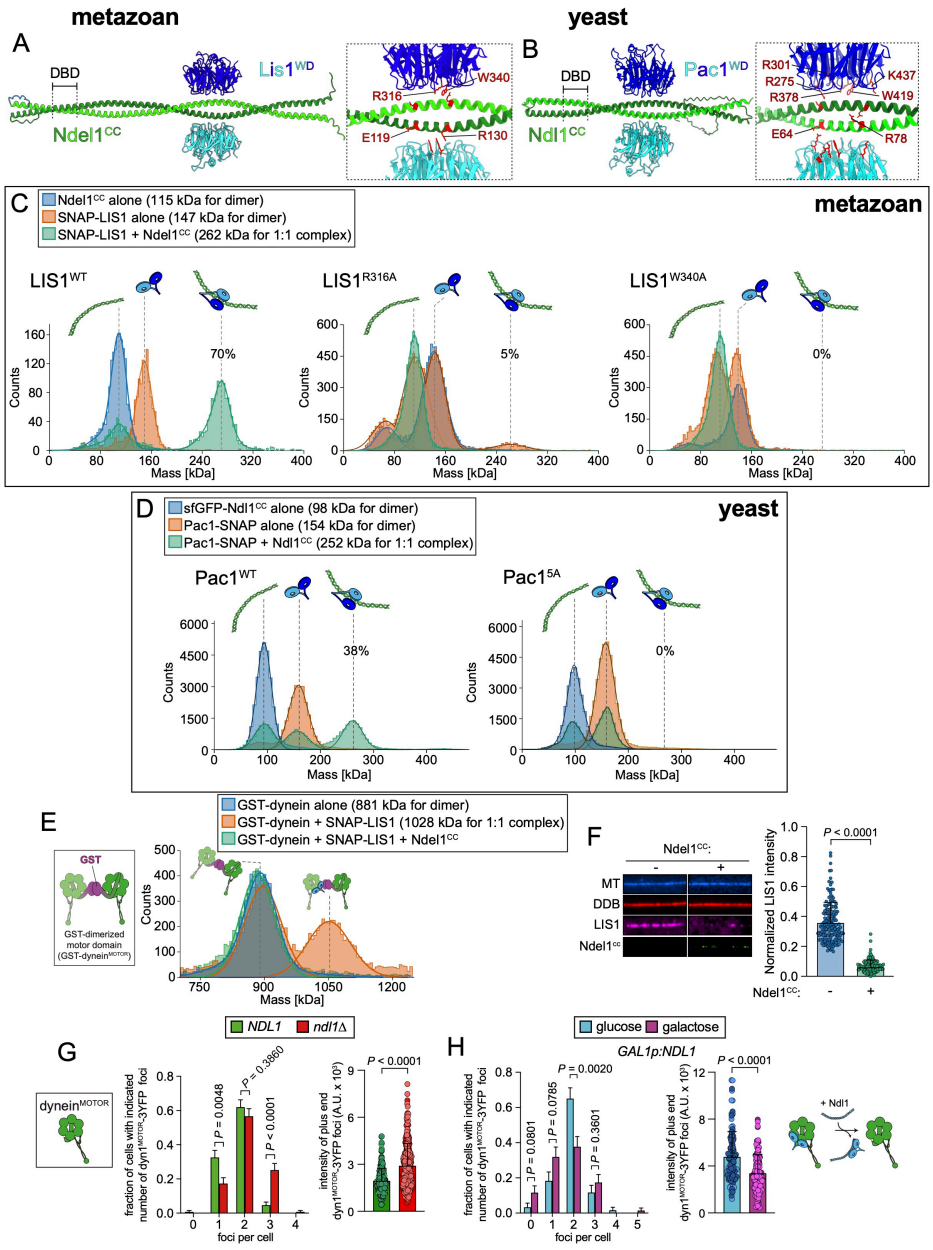

Figure 4. Dynein and Ndel1/Ndl1 compete for binding to LIS1/Pac1. A and B Alphafold2-Multimer models of 2 Ndl1^{CC}:2 Pac1^{WD40} **(A)** or 2 Ndel1^{CC}:2 LIS1^{WD40} **(B)** complexes (DBD, dynein-binding domain, as determined by mutagenesis (Wang and Zheng, 2011), see Fig. S3). Insets highlight residues on each protein mutated in this study or others (Gutierrez et al., 2017; Toropova et al., 2014; Wang and Zheng, 2011)). **C and D** Mass photometric analysis of individual proteins, or mixtures of proteins. Fits of mean mass values for each species, and relative fraction of particles (indicated on all plots for complexes) with indicated mass, are shown. Although the majority of species were comprised of 1:1 complexes, a minor but reproducible population of 2 Pac1:1 Ndl1 were apparent in all experiments with yeast proteins only (also see **Fig. S3E and F**). **E** Mass photometry of the human GST-dimerized dynein motor domain (depicted in cartoon schematic) with and without LIS1 and Ndel^{CC}. **F** Representative fluorescence images and quantitation depicting relative binding between microtubule-bound dynein-dynactin-BicD2 complexes (DDB) and LIS1 ± Ndel1^{CC} in the presence of AMPPNP (n = 88/71 microtubules for chambers without Ndel1^{CC}, and 57/68 microtubules for those with Ndel1^{CC}, from 2 independent replicates. *P* value calculated using one-way ANOVA test). **G and H** Plots depicting the extent of dynein^{MOTOR} localization in cells with and without Ndl1 (**G**; n = 129 *NDL1* and 127 *ndl1Δ* cells, and 113 and 130 foci from *NDL1* and *ndl1Δ* cells, respectively, all from 2 independent replicates), or with and without overexpressed Ndl1 (**E**; n = 60 uninduced, and 69 induced cells, and 116 and 114 foci from uninduced and induced cells, respectively, all from 2 independent replicates). *P* values were calculated using a Mann-Whitney test, or by calculating Z scores. For cells in panel **H**, which were engineered to possess a *GAL1* promoter upstream of the *NDL1* locus, Ndl1 overexpression was controlled by the exclusion or inclusion of galactose in the media for 3 hours immediately prior to imaging. Cartoon schematic in H depicts the proposed manner by which Ndl1 competes Pac1 away from dynein^{MOTOR}.

complex is an accurate structural model.

To validate the AF2 model of the corresponding yeast proteins, we generated mutations within Ndl1 and the N-terminus of Pac11 that would be predicted to disrupt ICN-Ndl1 interactions (Fig. S3B, "interface 1"), and Pac1-Ndl1 interactions (Fig. S3B, "interface 2"), and employed our TIRFM-based assay to assess their effects on protein interactions. Mutating a cluster of positively charged residues at interface 1 in the ICN to alanines (Pac11^{AAA}) strongly disrupted ICN-Ndl1 binding (Fig. S3C), while mutation of negatively charged residues at the N-terminus of the Ndl1 coiled-coil domain (Ndl1^{CC}) to alanines (Ndl1$^{CC[AAA]}$) also significantly impaired the Ndl1-dynein interaction (Fig. S3D). Using mass photometry, we found that interface 1 mutations on Ndl1 had no effect on its interaction with Pac1 (Fig. S3E). Finally, mutation of E64 and R78 at interface 2 of Ndl1^{CC} to alanines (analogous to E119 and R130 in Ndel1) disrupted Pac1 binding (Fig. S3F) but not dynein binding (Fig. S3G). These results verify the structural organization of the ICN-Ndl1 and Pac1-Ndl1 complexes predicted by AF2 and indicate that they are largely conserved from yeast to human.

Ndl1/Ndel1 competes with dynein for Pac1/LIS1 binding

Interestingly, the surface of the Pac1/LIS1 WD40 domain predicted to contact the Ndl1/Ndel1 coiled-coil overlaps with the reported dynein binding region of Pac1/LIS1 (Gutierrez et al., 2017; Toropova et al., 2014). This suggests that LIS1/Pac1 may only be able to bind to either Ndel1/Ndl1 or the dynein motor domain, but not both simultaneously. This observation contrasts with previous models that posited a tripartite Ndel1-LIS1-dynein motor complex (Huang et al., 2012; McKenney et al., 2010; Wang et al., 2013; Zylkiewicz et al., 2011). Competition between Ndl1 and dynein for Pac1/LIS1 potentially accounts for the reduction in dynein-LIS1/Pac1 binding we noted in Figure 3C and D at higher Ndel1/Ndl1 concentrations, which could be a consequence of excess Ndel1/Ndl1 in solution competitively binding to LIS1/Pac1.

To determine whether Pac1/LIS1 indeed employs the same surface to interact with Ndl1/Ndel1 and dynein, we assessed the ability of dynein-binding Pac1/LIS1 mutants (Gutierrez et al., 2017; Toropova et al., 2014) to interact with the coiled-coil regions of Ndl1 and Ndel1. We excluded the unstructured C-terminus of Ndel1/Ndl1 (see Fig. S3A and B) to assess whether this region is required for dynein-binding, as has been previously suggested (Liang et al., 2004; Sasaki et al., 2000). We mutated residues in Pac1 and LIS1 that have been shown to be important for dynein binding (R316A and W340A in LIS1; R275A, R301A, R378A, W419A, and K437A in Pac1; Fig. 4A and B), and employed mass photometry to assess complex formation. Whereas WT LIS1 and Pac1 both formed 1:1 dimeric complexes with Ndel1 and Ndl1 (Fig. 4C and D), the extent of complex formation was either strongly reduced, or eliminated by the mutations. In further support of the notion that LIS1 uses the same binding interface for both Ndel1 and dynein, Ndel1^{CC} effectively prevented LIS1 binding to a dimerized human dynein motor domain (dynein^{MOTOR}; which lacks the Ndel1-binding ICN; Fig. 4E), and preassembled dynein-dynactin-Bicd2 (DDB) complexes (Fig. 4F). To determine if the same competition occurs in live cells, we assessed the ability of Ndl1 to compete Pac1 away from a yeast dynein motor domain fragment (dynein^{MOTOR}) that is also lacking the ICN. Deletion of Ndl1 resulted in increased dynein^{MOTOR}-Pac1 binding (as apparent from the presence of plus end foci; Fig. 4G), while overexpression of Ndl1 had the opposite effect (i.e., reduced the frequency and intensity of dynein^{MOTOR} foci; Fig. 4H). Taken together, these data indicate that the coiled-coil domain of Ndel/Ndl1 and the dynein ICN compete for LIS1/Pac1 binding, suggesting that Ndel1/Ndl1-recruited LIS1/Pac1 must first unbind from Ndel1/Ndl1 prior to binding to the motor domain.

Competitive binding of p150^{CC1} or Ndel1 to the ICN precludes DDA assembly

A well-established method to inhibit dynein function in cells involves microinjection or expression of p150^{CC1} in mammalian cells (Quintyne et al., 1999). Although this technique has been used in numerous studies, the mechanism by which this truncated protein precludes dynein function is unknown, as it does not disrupt dynactin integrity (King et al., 2003). In light of our findings that this fragment makes direct contacts with the ICN, we hypothesized that p150^{CC1} competes for ICN binding with the native p150 molecule in the dynactin complex. We first wondered whether expression of p150^{CC1} also inhibits dynein function in budding yeast. To this end, we generated yeast strains engineered to conditionally overexpress Nip100^{CC1} from the galactose-inducible *GAL1* promoter (*GAL1p*). In contrast to uninduced cells, a large fraction of those overexpressing Nip100^{CC1} possessed a mispositioned spindle, indicating that the capacity to disrupt dynein activity by this fragment is indeed conserved (Fig. 5A). We observed Nip100^{CC1} colocalizing to the SPBs and to microtubule plus ends with dynein (Fig. 5B, arrowheads, and arrow, respectively), indicative of their binding in cells.

To directly test whether p150^{CC1} competitively inhibits dynein-dynactin binding, we assessed the extent of DDA complex assembly in the absence or presence of this protein fragment. We also included recombinant LIS1 in our assays given its recently documented ability to promote DDA complex assembly (Elshenawy et al., 2020; Marzo. et al., 2020; Qiu et al., 2019; Zaw Min Htet, 2020). Using the purified cargo adapter Hook3, we quantified the extent of DDH assembly in bovine brain lysate by affinity isolation (Fig. 5C). In the absence of p150^{CC1}, the addition of LIS1 promoted DDA assembly (by ~3-fold; Fig. 5D), consistent

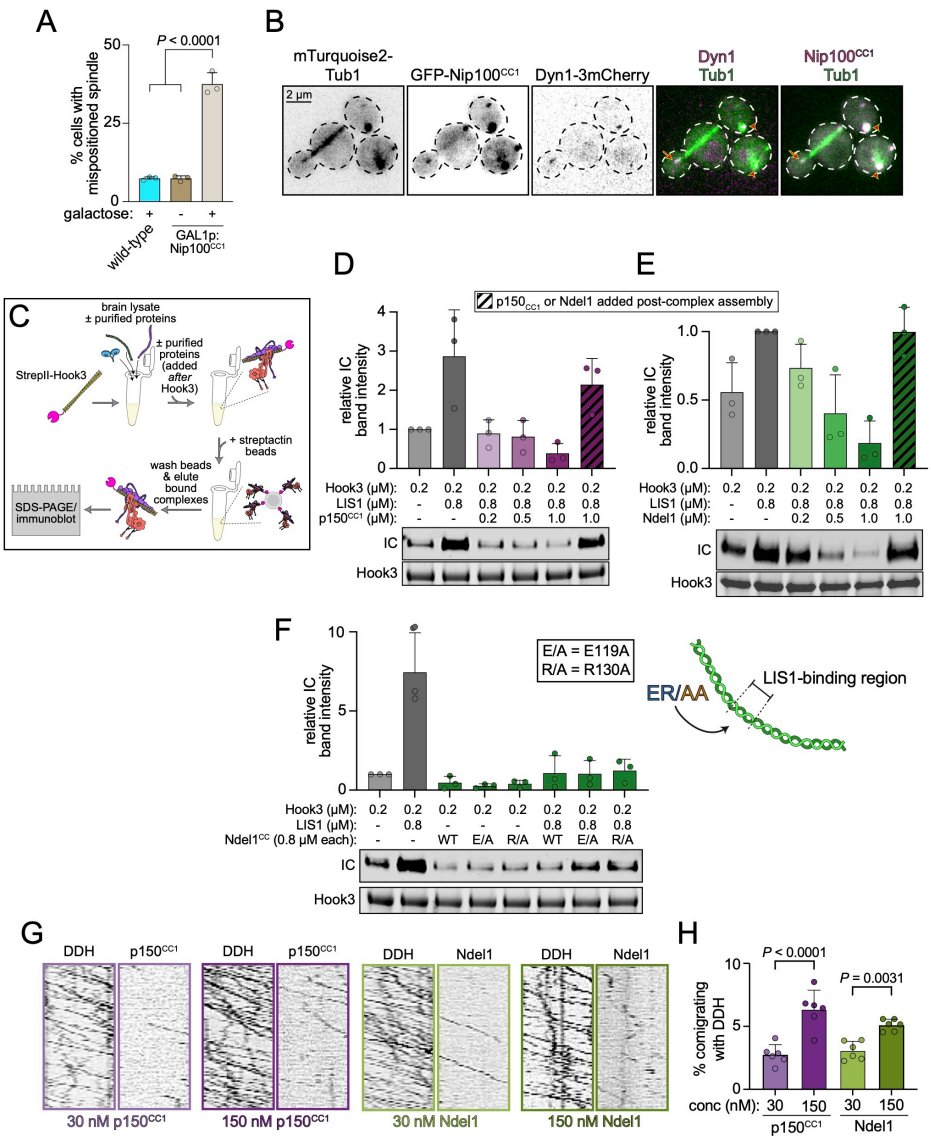

Figure 5. Excess p150^{CC1} and Ndel1 competitively inhibit DDA assembly but do not perturb pre-assembled complexes. A The fraction of cells with a mispositioned spindle are plotted (mean ± SD, along with values from individual replicates; n = 53/64/44 WT + galactose cells, 26/62/31 + glucose Gal1p:Nip100^{CC1}cells, and 50/60/43 + galactose Gal1p:Nip100^{CC1} cells, all from 3 independent replicates). *P* values were generated by calculating Z scores. **B** Representative fluorescence images of Nip100^{CC1}-overexpressing cells (after growth in galactose-containing media) depicting localization of Nip100^{CC1} within cells (arrows, plus end foci; arrowheads, SPB foci). **C** Cartoon schematic depicting experimental strategy to assess DDA complex formation in the absence or presence of indicated recombinant proteins, added either prior to addition of Hook3 to lysates, or 60 minutes thereafter. **D - F** Immunoblots and plots depicting relative degree of DDH assembly as a consequence of addition of indicated wild-type factors **(D and E)**, or indicated mutant Ndel1^{CC} (**F**). **G** Representative kymographs from two-color movies depicting motility of 30 nM DDH complexes (assembled as indicated in panel **C**) in the presence of indicated concentration of fluorescent p150^{CC1} or Ndel1. Note the low frequency of comigration of p150^{CC1} and Ndel1 with DDH. **H** Plot (mean ± SD, along with values from independent replicates) depicting frequency of comigration of p150^{CC1} or Ndel1 with DDH complexes (n = 646/837/698/539/542/243, 512/1020/449/646/670/558, 775/664/978/486/412/516, 2188/860/770/328/537/349 processively migrating DDH particles for 30 nM and 150 nM p150^{CC1}, 30 nM and 150 nM Ndel1, respectively. *P* values were calculated using one-way ANOVA).

with recent reports. However, titration of increasing amounts of p150^{CC1} significantly compromised this process, suggesting that p150^{CC1} indeed competitively disrupts dynein-dynactin binding. We next wondered whether p150^{CC1} could effectively compete with endogenous p150 for ICN binding after DDA complex assembly was already complete. To this end, we repeated our assay, but instead of including p150^{CC1} coincident with LIS1 and Hook3, we added p150^{CC1} 60 minutes after Hook3 addition. Interestingly, this led to almost no disruption in DDA assembly (Fig. 5D, hatched bar), suggesting that native p150 within the dynactin complex either exhibits higher affinity for dynein than the isolated p150^{CC1} fragment, or that p150^{CC1}-ICN binding is not required to maintain assembled DDA complexes.

Previous studies have revealed that human p150^{CC1} and Ndel1 compete for binding to the ICN (McKenney et al., 2011; Nyarko et al., 2012), suggesting excess Ndel1 may also inhibit DDA assembly in vitro. Using our TIRFM-based binding assay, we found that yeast Nip100^{CC1} and Ndl1 both exhibit similarly high affinity for the dynein complex (Fig. S4A), and compete for binding to dynein (Fig. S4B), much like their human counterparts. Moreover, we found that Ndl1 bound equally well to both WT yeast dynein, which exists predominantly in the phi conformation, and a mutant "open" dynein that cannot adopt the phi conformation (dynein^{DK}, Fig. S4A) (Marzo. et al., 2020). This is in contrast to Pac1, which exhibits a greater degree of binding to the open mutant than WT, as expected (Fig. S4C) (Marzo. et al., 2020).

In light of the in vivo data indicating an important role for Ndl1 in promoting dynein localization and function in yeast (Fig. 3D and S2) (Li et al., 2005), we wondered whether inclusion of Ndel1 in our DDA assembly assay would enhance LIS1 activity (i.e., increase DDA assembly), or whether its binding to the ICN would compete with p150 binding, and thus preclude complex assembly, similar to p150^{CC1}. To this end, we repeated our assay above (Fig. 5C) with increasing concentrations of Ndel1, which caused a dose-dependent decrease in DDA assembly (Fig. 5E). We noted that higher concentrations of Ndel1 were required to achieve similar degrees of complex disruption, suggesting that p150^{CC1} may have higher affinity for ICN than Ndel1. Using our TIRFM-based binding assay, we

found this to be the case, with $p150^{CC1}$ exhibiting a ~6-fold greater apparent affinity for dynein than Ndel1 (Fig. S4D). Finally, as noted above for $p150^{CC1}$, addition of Ndel1 to lysates 60 minutes after addition of Hook3 did not disrupt DDA complex assembly (Fig. 5E, hatched bar). Thus, despite Ndel1's in-cell activity, which is to promote dynein-LIS1 binding, its excess in vitro perturbs DDA assembly in a manner similar to $p150^{CC1}$.

We wondered whether this inhibitory activity of Ndel1 is due to sequestration of either native or recombinant LIS1 in the lysates, thus preventing dynein-LIS1 binding. To test this, we repeated our DDA assembly assay using Ndel1 mutants that are unable to bind LIS1, but competent for interaction with dynein: E119A and R130A (see Fig. 4A, inset) (Derewenda et al., 2007). We used the coiled-coil fragment of Ndel1, which is sufficient to interact with LIS1 (Tarricone et al., 2004) (Fig. 4C). Inclusion of these mutants in the lysate concurrent with Hook3 prevented DDA assembly to the same extent as WT $Ndel1^{CC}$, indicating this inhibition is likely a consequence of $Ndel1^{CC}$-ICN binding, and not the result of LIS1 sequestration. Considering the similar degree of inhibition by $Ndel1^{CC}$ and full-length Ndel1 (compare Fig. 5E and 5F), these data further indicate that the C-terminus of Ndel1 is not required for its interaction with dynein.

Finally, we wondered why preassembled DDA complexes were refractory to Ndel1 and $p150^{CC1}$-mediated inhibition. We hypothesized that this was a consequence of one of two possible scenarios: (1) the $p150^{CC1}$-ICN contact is only required for assembly, but not for maintenance of assembled DDA complexes; or, (2) the ICN-$p150^{CC1}$ contacts are required for maintenance of the complex, but become sufficiently stabilized (possibly due to the avidity provided by HC-dynactin interactions) such that exogenous $p150^{CC1}$ or Ndel1 are no longer able to compete for binding. TIRFM imaging of single molecules of preassembled DDH complexes mixed with either fluorescent Ndel1 or $p150^{CC1}$ revealed that a very small proportion of motile DDH complexes colocalized with either Ndel1 or $p150^{CC1}$ across a five-fold range of concentrations (Fig. 5G and H). We interpret the lack of robust $p150^{CC1}$ or Ndel1 binding to motile DDH complexes as an indication that the ICN is stably bound to the p150 coiled-coil within the dynactin complex, and thus unable to interact with the exogenous polypeptides.

Discussion

In this work, we find a remarkably limited region of the overall ~1.4 MDa cytoplasmic dynein complex is required for the activation of dynein motility by dynactin and cargo adapters both in vitro and in cells. While a direct interaction between the ICN and p150 was identified over 25 years ago (Vaughan and Vallee, 1995), its role in dynein function has remained elusive, even after the revelation of recent high resolution cryo-EM structures of assembled DDA complexes (Chaaban and Carter, 2022; Urnavicius et al., 2018; Urnavicius et al., 2015). Our results reveal a conserved role for this interaction that spans over a billion years of evolution. In the absence of the ICN-p150 interaction, dynein is unable to interact with dynactin and cargo adapters, leading to behaviors that phenocopy the complete loss of dynein activity in cells. Our data explain long-standing observations in the dynein field. First, the mechanism of $p150^{CC1}$ as an inhibitor of dynein function in cells can be explained by our finding of a competitive interaction with the endogenous p150 within the dynactin complex for the dynein ICN. Second, excess Ndel1 disrupts dynein function in mitotic spindle assembly (Wang et al., 2013) and vesicular trafficking (Liang et al., 2004), likely because it competes with p150 during DDA assembly. Third, monoclonal antibodies that recognize the ICN (McKenney et al., 2011) disrupt dynein transport in vivo (Burkhardt et al., 1995; Roossien et al., 2014; Yi et al., 2011), likely through perturbation of DDA assembly as shown here for both Ndel1 and $p150^{CC1}$, which also bind to the ICN. Finally, our data explain why Ndel1 acts as a positive modulator of dynein activity in both genetic and cell biological experiments (Bruno et al., 1996; Li et al., 2005; Minke et al., 1999; Raaijmakers et al., 2013; Zhang et al., 2009), via its role in the direct recruitment of the dynein activator, LIS1, to the motor.

Despite much attention in the field, the precise roles of the ubiquitous and critical dynein regulators LIS1 and Ndel1 have remained opaque (Garrott et al., 2022; Markus et al., 2020). The relatively recent discoveries of the dynein autoinhibition and activation pathways (Markus et al., 2020; Reck-Peterson et al., 2018) have provided new context for possible roles of these molecules in dynein function. Recent work by several groups revealed LIS1's role in biasing the formation of activated DDA complexes by interfering with the autoinhibited phi conformation of the dynein dimer via its interactions with the dynein motor domain (Elshenawy et al., 2020; Marzo. et al., 2020; Qiu et al., 2019; Zaw Min Htet, 2020). LIS1 binding is thought to stabilize the open conformation of the motor by acting as a "check valve" that prevents reversion of dynein back to the autoinhibited phi conformation, thus priming it for assembly with dynactin and cargo adapters (Markus et al., 2020). However, the function of Ndel1 in this dynein activation process has remained unclear. Our current data confirm prior results suggesting a role for Ndel1 in the recruitment of LIS1 to the dynein motor via Ndel1's interaction with the ICN (Fig. 6). Our biochemical and cell biological data fit well with previous data suggesting that Ndel1 promotes LIS1 function in a range of model systems, from fungi to metazoa (Efimov and Morris, 2000; Garrott et al., 2022; Li et al., 2005; Moon et al., 2014). For example, it has been noted by several groups that Ndel1 depletion (or deletion) phenotypes can be rescued by LIS1 overexpression. Interestingly, the converse has also been noted: that Ndel1 overexpression can rescue LIS1 depletion – but not deletion – phenotypes (Efimov and Morris, 2000; Lam et al., 2010). These latter data are likely also explained by Ndel1 recruitment of LIS1 to dynein,

thereby increasing the effective LIS1 concentration with respect to dynein. As haploinsufficiency of LIS1 causes lissencephaly, the cellular concentration of LIS1 is critical for human health. Thus, the recruitment of LIS1 to dynein by Ndel1 likely plays a key role in ensuring proper dynein activity and cellular homeostasis.

Prior models posited that Ndel1 recruits LIS1 to dynein through simultaneous binding of LIS1 to both Ndel1 and the dynein motor domain (McKenney et al., 2010; Wang et al., 2013; Zylkiewicz et al., 2011). However, our new data challenges this notion, and instead supports a model in which LIS1 must unbind from Ndel1 prior to binding to dynein. In addition to scaffolding dynein and LIS1 within a single protein complex, this model suggests that Ndel1 may also function to prevent LIS1 from binding directly to the dynein motor domain in a temporally discrete step that precedes LIS1-induced dynein activation, as recently proposed by Garrott and colleagues (Fig. 6, steps 2 and 3) (Garrott et al., 2022). In this model, a yet unknown mechanism may trigger a "hand off" of LIS1 from Ndel1 onto the dynein motor domain, thus initiating LIS1-induced activation of DDA assembly. One such trigger may be the switch of dynein from its phi state – to which LIS1 cannot bind– to its open state to which LIS1 binds well (Marzo. et al., 2020; Zaw Min Htet, 2020). Alternatively, competitive binding of p150 to the ICN, which causes Ndel1-ICN unbinding, could potentially also disrupt Ndel1-LIS1 binding, facilitating the hand-off of LIS1 to the motor domain (Fig. 6, step 3). Post-translational modification may also play a role. For example, Ndel1 is known to be phosphorylated on several residues (Garrott et al., 2022), with one study showing weakened LIS1 binding as a consequence (Bradshaw et al., 2011).

What role does the ICN-p150 interaction play in DDA assembly? Cryo-EM and cross-linking coupled with mass spectrometry data have revealed that the elongated p150 projection arm folds back onto dynactin's actin-related protein 1 (Arp1) filament to interact with the pointed end of the dynactin complex (Lau et al., 2021; Urnavicius et al., 2015) (see Fig. 6). In this conformation, the p150 arm occludes the interaction of cargo adapter proteins with the Arp1 filament, resulting in an autoinhibited dynactin (Fig. 6, step 3) (Lau et al., 2021). Contacts have also been identified between $p150^{CC1a}$ and $p150^{CC1b}$ (Tripathy et al., 2014). Although unclear, this latter interaction may also play a role in maintaining the autoinhibited conformation of dynactin (see Fig. 6 inset with CC1a/1b). This model is consistent with single molecule observations that dynactin does not robustly interact with microtubules in isolation, whereas isolated p150 does (McKenney et al., 2016). Therefore, we speculate that the interaction between ICN and $p150^{CC1b}$ may represent the initial contact between dynein and dynactin that stimulates the release of the autoinhibited conformation of the p150 projection arm (Fig. 6, step 4), priming assembly of the fully active DDA complex (Fig. 6, step 5). However, our data also revealed that exogenous Ndel1 or $p150^{CC1}$ do not disrupt the integrity of preassembled DDH complexes, and do not robustly associate with processively moving DDH complexes. These data suggest that within the context of the fully assembled DDA complex, the ICN is stably bound to p150 within the dynactin complex during dynein motility. Therefore, we conclude that the ICN-p150 interaction is not only required

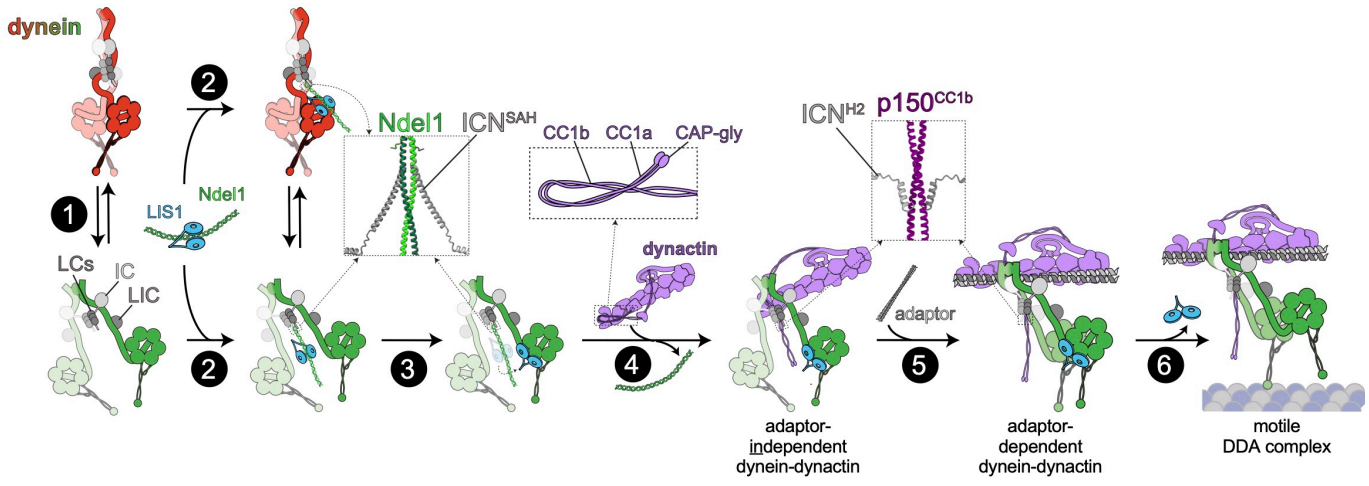

Figure 6. Model for dynein activation. 1 Dynein stochastically switches between the autoinhibited 'phi' and open states. **2** Ndel1 binding to the ICN SAH (Nyarko et al., 2012), which binds equally well to the phi and open states (Fig. **S4A**), recruits LIS1 to dynein. **3** An unknown mechanism leads to LIS1 unbinding from Ndel1, and binding to open dynein, thus stabilizing this conformation. **4** Interactions between H2 of the ICN and $p150^{CC1b}$ (Morgan et al., 2011; Nyarko et al., 2012) competitively inhibit ICN-Ndel1 binding (McKenney et al., 2011), initiate dynein-dynactin binding (independent of a cargo adaptor), and potentially relieves dynactin autoinhibition (the latter of which is due to interactions between $p150^{CC1}$ and the pointed end complex) (Lau et al., 2021). **5** Binding of a cargo adaptor to the adaptor-independent dynein-dynactin complex, which requires ICN-p150 binding, leads to assembly of the active dynein-dynactin-adaptor (DDA) complex. Insets show AF2 models of human ICN with either Ndel1 or $p150^{CC1}$. Note that data suggests that the ICN-p150 interaction involves both the SAH and H2 of ICN (Nyarko et al., 2012), but only the AF2 predicted H2-p150 interaction is shown here. **6** Coincident with microtubule binding, LIS1 dissociates (Ton et al., 2022), and the active DDA complex processively transports cargoes along microtubules.

for initiation of DDA assembly, but is also a sustained contact within the fully assembled DDA complex.

We propose the following model to incorporate our data into the existing understanding of dynein activation. Dynein exists in equilibrium between the autoinhibited phi and open conformations (Fig. 6, step 1). Although we find that Ndl1 binds equally well to either conformation in vitro (Fig. S4A), it remains to be determined if Ndl1/Ndel1 affects the equilibrium between these two conformations. Binding of Ndel1 to the SAH of the ICN (Fig. S1b) (Jie et al., 2015; Nyarko et al., 2012) recruits LIS1 to dynein, while simultaneously preventing LIS1 engagement with the dynein motor domain (Fig. 6, step 2). An unknown mechanism triggers the dissociation of LIS1 from Ndel1, and its subsequent interaction with the open form of the dynein motor, possibly concurrent with the dissociation of Ndel1 from the ICN. We propose that the interaction of the SAH and H2 of the ICN (Fig. S1b) with dynactin-bound $p150^{CC1b}$ (Jie et al., 2015; Loening et al., 2020; Morgan et al., 2011; Nyarko et al., 2012) relieves dynactin autoinhibition by preventing CC1 from contacting the dynactin pointed end, or by potentially interfering with the CC1a-CC1b interaction (Tripathy et al., 2014) (Fig. 6, step 4). The resulting open dynein-LIS1-dynactin complex is not capable of processive motility, but is primed for interaction with a cargo-adaptor molecule. This adapter-independent dynein-dynactin-LIS1 complex may represent the plus-end bound dynein complexes observed in yeast and metazoans (Baumbach et al., 2017; Jha et al., 2017; Lee et al., 2003; Moore et al., 2008; Splinter et al., 2012). This complex binds to one of the growing number of dynein cargo-adapters (Reck-Peterson et al., 2018), which themselves are bound to various cellular cargos, leading to the formation of the active DDA complex that is competent for processive motility (Fig. 6, step 5; cargo not shown for clarity). Data indicates that LIS1 dissociates from the DDA complex as a consequence of dynein-microtubule binding immediately prior to commencement of motility (Egan et al., 2012; Elshenawy. et al., 2020; Lammers and Markus, 2015; Ton et al., 2022; Zaw Min Htet, 2020) (Fig. 6, step 6). Although LIS1 has been observed comigrating with processively moving DDA complexes in vitro (Baumbach et al., 2017; Gutierrez et al., 2017), it is unclear if these LIS1 molecules are bound to those dynein motors directly engaged with the microtubule, or possibly to a second dynein dimer scaffolded within the motile DDA complex that is not engaged directly in motility. In summary, our results provide new insights into previously unknown steps in the dynein activation pathway, provide a new model for the mysterious role of Ndel1 in the dynein pathway, and reveal a critical, evolutionarily conserved role of the ICN in the activation of dynein in vivo.

References

Alkuraya, F.S., Cai, X., Emery, C., Mochida, G.H., Al-Dosari, M.S., Felie, J.M., Hill, R.S., Barry, B.J., Partlow, J.N., Gascon, G.G., et al. (2011). Human mutations in NDE1 cause extreme microcephaly with lissencephaly [corrected]. Am J Hum Genet 88, 536-547.

Amos, L.A. (1989). Brain dynein crossbridges microtubles into bundles. J Cell Sci 93, 19-28.

Bakircioglu, M., Carvalho, O.P., Khurshid, M., Cox, J.J., Tuysuz, B., Barak, T., Yilmaz, S., Caglayan, O., Dincer, A., Nicholas, A.K., et al. (2011). The essential role of centrosomal NDE1 in human cerebral cortex neurogenesis. Am J Hum Genet 88, 523-535.

Baumbach, J., Murthy, A., McClintock, M.A., Dix, C.I., Zalyte, R., Hoang, H.T., and Bullock, S.L. (2017). Lissencephaly-1 is a context-dependent regulator of the human dynein complex. eLife 6.

Bradshaw, N.J., Soares, D.C., Carlyle, B.C., Ogawa, F., Davidson-Smith, H., Christie, S., Mackie, S., Thomson, P.A., Porteous, D.J., and Millar, J.K. (2011). PKA phosphorylation of NDE1 is DISC1/PDE4 dependent and modulates its interaction with LIS1 and NDEL1. J Neurosci 31, 9043-9054.

Bruno, K.S., Tinsley, J.H., Minke, P.F., and Plamann, M. (1996). Genetic interactions among cytoplasmic dynein, dynactin, and nuclear distribution mutants of Neurospora crassa. Proc Natl Acad Sci U S A 93, 4775-4780.

Burkhardt, J.K., Echeverri, C.J., and Vallee, R.B. (1995). Overexpression of the p50 subunit of dynactin perturbs the positioning of the golgi apparatus and endosomes. Mol Biol Cell 6, 266a.

Carminati, J.L., and Stearns, T. (1997). Microtubules orient the mitotic spindle in yeast through dynein-dependent interactions with the cell cortex. J Cell Biol 138, 629-641.

Carter, A.P., Diamant, A.G., and Urnavicius, L. (2016). How dynein and dynactin transport cargos: a structural perspective. Curr Opin Struct Biol 37, 62-70.

Chaaban, S., and Carter, A.P. (2022). Structure of dynein-dynactin on microtubules shows tandem adaptor binding. Nature 610, 212-216.

Chandradoss, S.D., Haagsma, A.C., Lee, Y.K., Hwang, J.H., Nam, J.M., and Joo, C. (2014). Surface passivation for single-molecule protein studies. J Vis Exp.

Derewenda, U., Tarricone, C., Choi, W.C., Cooper, D.R., Lukasik, S., Perrina, F., Tripathy, A., Kim, M.H., Cafiso, D.S., Musacchio, A., et al. (2007). The structure of the coiled-coil domain of Ndel1 and the basis of its interaction with Lis1, the causal protein of Miller-Dieker lissencephaly. Structure 15, 1467-1481.

Duellberg, C., Trokter, M., Jha, R., Sen, I., Steinmetz, M.O., and Surrey, T. (2014). Reconstitution of a hierarchical +TIP interaction network controlling microtubule end tracking of dynein. Nat Cell Biol 16, 804-811.

Echeverri, C.J., Paschal, B.M., Vaughan, K.T., and Vallee, R.B. (1996). Molecular characterization of the 50-kD subunit of dynactin reveals function for the complex in chromosome alignment and spindle organization during mitosis. J Cell Biol 132, 617-633.

Ecklund, K.H., Bailey, M.E., Kossen, K.A., Dietvorst, C.K., Asbury, C.L., and Markus, S.M. (2021). The microtubule-associated protein She1 coordinates directional spindle positioning by spatially restricting dynein activity. J Cell Sci 134.

Ecklund, K.H., Marzo, M.G., and Markus, S.M. (2023). Using Budding Yeast as a Model to Understand Dynein-Mediated Cargo Transport. Methods Mol Biol 2623, 25-42.

Ecklund, K.H., Morisaki, T., Lammers, L.G., Marzo, M.G., Stasevich, T.J., and Markus, S.M. (2017). She1 affects dynein through direct interactions with the microtubule and the dynein microtubule-binding domain. Nat Commun 8, 2151.

Efimov, V.P., and Morris, N.R. (2000). The LIS1-related NUDF protein of Aspergillus nidulans interacts with the coiled-coil domain of the NUDE/RO11 protein. J Cell Biol 150, 681-688.

Egan, M.J., Tan, K., and Reck-Peterson, S.L. (2012). Lis1 is an initiation factor for dynein-driven organelle transport. J Cell Biol 197, 971-982.

Elshenawy, M.M., Kusakci, E., Volz, S., Baumbach, J., Bullock, S.L., and Yildiz, A. (2020). Lis1 activates dynein motility by modulating its pairing with dynactin. Nat Cell Biol 22, 570-578.

Elshenawy., M.M., Kusakci., E., Volz., S., Baumbach., J., Bullock., S.L., and Yildiz., A. (2020). LIS1 Activates Dynein Motility by Pairing it with Dynactin. Nature cell biology.

Eshel, D., Urrestarazu, L.A., Vissers, S., Jauniaux, J.C., van Vliet-Reedijk, J.C., Planta, R.J., and Gibbons, I.R. (1993). Cytoplasmic dynein is required for normal nuclear segregation in yeast. Proc Natl Acad Sci U S A 90, 11172-11176.

Fiorillo, C., Moro, F., Yi, J., Weil, S., Brisca, G., Astrea, G., Severino, M., Romano, A., Battini, R., Rossi, A., et al. (2014). Novel dynein DYNC1H1 neck and motor domain mutations link distal spinal muscular atrophy and abnormal cortical development. Human mutation 35, 298-302.

Gaglio, T., Saredi, A., Bingham, J.B., Hasbani, J., Gill, S.R., Schroer, T.A., and Compton, D.A. (1996). Opposing motor activities are required for the organization of the mammalian mitotic spindle pole. J Cell Biol 135, 399-414.

Garrott, S.R., Gillies, J.P., and DeSantis, M.E. (2022). Nde1 and Ndel1: Outstanding Mysteries in Dynein-Mediated Transport. Front Cell Dev Biol 10, 871935.

Gutierrez, P.A., Ackermann, B.E., Vershinin, M., and McKenney, R.J. (2017). Differential effects of the dynein-regulatory factor Lissencephaly-1 on processive dynein-dynactin motility. J Biol Chem.

Guven, A., Gunduz, A., Bozoglu, T.M., Yalcinkaya, C., and Tolun, A. (2012). Novel NDE1 homozygous mutation resulting in microhydranencephaly and not microlyssencephaly. Neurogenetics 13, 189-194.

Ha, J., Lo, K.W., Myers, K.R., Carr, T.M., Humsi, M.K., Rasoul, B.A., Segal, R.A., and Pfister, K.K. (2008). A neuron-specific cytoplasmic dynein isoform preferentially transports TrkB signaling endosomes. J Cell Biol 181, 1027-1039.

Heald, R., Tournebize, R., Blank, T., Sandaltzopoulos, R., Becker, P., Hyman, A., and Karsenti, E. (1996). Self-organization of microtubules into bipolar spindles around artificial bipolar spindles around artifical chromosomes in Xenopus egg extracts. Nature 382, 420-425.

Huang, J., Roberts, A.J., Leschziner, A.E., and Reck-Peterson, S.L. (2012). Lis1 acts as a "clutch" between the ATPase and microtubule-binding domains of the dynein motor. Cell 150, 975-986.

Jha, R., Roostalu, J., Trokter, M., and Surrey, T. (2017). Combinatorial Regulation Of The Balance Between Dynein Microtubule End Accumulation And Initiation Of Directed Motility. bioRxiv.

Jie, J., Lohr, F., and Barbar, E. (2015). Interactions of Yeast Dynein with Dynein Light Chain and Dynactin: GENERAL IMPLICATIONS FOR INTRINSICALLY DISORDERED DUPLEX SCAFFOLDS IN MULTIPROTEIN ASSEMBLIES. J Biol Chem 290, 23863-23874.

Jie, J., Lohr, F., and Barbar, E. (2017). Dynein Binding of Competitive Regulators Dynactin and NudE Involves Novel Interplay between Phosphorylation Site and Disordered Spliced Linkers. Structure 25, 421-433.

Jumper, J., Evans, R., Pritzel, A., Green, T., Figurnov, M., Ronneberger, O., Tunyasuvunakool, K., Bates, R., Zidek, A., Potapenko, A., et al. (2021). Highly accurate protein structure prediction with AlphaFold. Nature 596, 583-589.

Karki, S., and Holzbaur, E.L.F. (1995). Affinity chromatography demonstrates a direct binding between cytoplasmic dynein and the dynactin complex. J Biol Chem 270, 28806-28811.

King, S.J., Brown, C.L., Maier, K.C., Quintyne, N.J., and Schroer, T.A. (2003). Analysis of the dynein-dynactin interaction in vitro and in vivo. Mol Biol Cell 14, 5089-5097.

Knop, M., Siegers, K., Pereira, G., Zachariae, W., Winsor, B., Nasmyth, K., and Schiebel, E. (1999). Epitope tagging of yeast genes using a PCR-based strategy: more tags and improved practical routines. Yeast 15, 963-972.

Lam, A.J., Rao, L., Anazawa, Y., Okada, K., Chiba, K., Dacy, M., Niwa, S., Gennerich, A., Nowakowski, D.W., and McKenney, R.J. (2021). A highly conserved 3(10) helix within the kinesin motor domain is critical for kinesin function and human health. Sci Adv 7.

Lam, C., Vergnolle, M.A., Thorpe, L., Woodman, P.G., and Allan, V.J. (2010). Functional interplay between LIS1, NDE1 and NDEL1 in dynein-dependent organelle positioning. J Cell Sci 123, 202-212.

Lammers, L.G., and Markus, S.M. (2015). The dynein cortical anchor Num1 activates dynein motility by relieving Pac1/LIS1-mediated inhibition. J Cell Biol 211, 309-322.

Lau, C.K., O'Reilly, F.J., Santhanam, B., Lacey, S.E., Rappsilber, J., and Carter, A.P. (2021). Cryo-EM reveals the complex architecture of dynactin's shoulder region and pointed end. EMBO J 40, e106164.

Lee, W.L., Oberle, J.R., and Cooper, J.A. (2003). The role of the lissencephaly protein Pac1 during nuclear migration in budding yeast. J Cell Biol 160, 355-364.

Li, J., Lee, W.L., and Cooper, J.A. (2005). NudEL targets dynein to microtubule ends through LIS1. Nat Cell Biol 7, 686-690.

Li, Y.Y., Yeh, E., Hays, T., and Bloom, K. (1993). Disruption of mitotic spindle orientation in a yeast dynein mutant. Proc Natl Acad Sci U S A 90, 10096-10100.

Liang, Y., Yu, W., Li, Y., Yang, Z., Yan, X., Huang, Q., and Zhu, X. (2004). Nudel functions in membrane traffic mainly through association with Lis1 and cytoplasmic dynein. J Cell Biol 164, 557-566.

Loening, N.M., Saravanan, S., Jespersen, N.E., Jara, K., and Barbar, E. (2020). Interplay of Disorder and Sequence Specificity in the Formation of Stable Dynein-Dynactin Complexes. Biophys J 119, 950-965.

Longtine, M.S., McKenzie, A., 3rd, Demarini, D.J., Shah, N.G., Wach, A., Brachat, A., Philippsen, P., and Pringle, J.R. (1998). Additional modules for versatile and economical PCR-based gene deletion and modification in Saccharomyces cerevisiae. Yeast 14, 953-961.

Makokha, M., Hare, M., Li, M., Hays, T., and Barbar, E. (2002). Interactions of cytoplasmic dynein light chains Tctex-1 and LC8 with the intermediate chain IC74. Biochemistry 41, 4302-4311.

Markus, S.M., Kalutkiewicz, K.A., and Lee, W.L. (2012). She1-mediated inhibition of dynein motility along astral microtubules promotes polarized spindle movements. Curr Biol 22, 2221-2230.

Markus, S.M., and Lee, W.L. (2011). Regulated offloading of cytoplasmic dynein from microtubule plus ends to the cortex. Dev Cell 20, 639-651.

Markus, S.M., Marzo, M.G., and McKenney, R.J. (2020). New insights into the mechanism of dynein motor regulation by lissencephaly-1. Elife 9.

Markus, S.M., Omer, S., Baranowski, K., and Lee, W.L. (2015). Improved Plasmids for Fluorescent Protein Tagging of Microtubules in Saccharomyces cerevisiae. Traffic 16, 773-786.

Markus, S.M., Plevock, K.M., St Germain, B.J., Punch, J.J., Meaden, C.W., and Lee, W.L. (2011). Quantitative analysis of Pac1/LIS1-mediated dynein targeting: Implications for regulation of dynein activity in budding yeast. Cytoskeleton 68, 157-174.

Markus, S.M., Punch, J.J., and Lee, W.L. (2009). Motor- and tail-dependent targeting of dynein to microtubule plus ends and the cell cortex. Curr Biol 19, 196-205.

Marzo, M.G., Griswold, J.M., Ruff, K.M., Buchmeier, R.E., Fees, C.P., and Markus, S.M. (2019). Molecular basis for dyneinopathies

reveals insight into dynein regulation and dysfunction. eLife 8.
Marzo., M.G., Griswold., J.M., and Markus, S.M. (2020). Pac1/LIS1 Stabilizes an Uninhibited Conformation of Dynein to Coordinate its Localization and Activity. Nature cell biology.
McKenney, R.J., Huynh, W., Tanenbaum, M.E., Bhabha, G., and Vale, R.D. (2014). Activation of cytoplasmic dynein motility by dynactin-cargo adapter complexes. Science 345, 337-341.
McKenney, R.J., Huynh, W., Vale, R.D., and Sirajuddin, M. (2016). Tyrosination of alpha-tubulin controls the initiation of processive dynein-dynactin motility. Embo J.
McKenney, R.J., Vershinin, M., Kunwar, A., Vallee, R.B., and Gross, S.P. (2010). LIS1 and NudE Induce a Persistent Dynein Force-Producing State. Cell 141, 304-316.
McKenney, R.J., Weil, S.J., Scherer, J., and Vallee, R.B. (2011). Mutually exclusive cytoplasmic dynein regulation by NudE-Lis1 and dynactin. J Biol Chem 286, 39615-39622.
Minke, P.F., Lee, I.H., Tinsley, J.H., Bruno, K.S., and Plamann, M. (1999). Neurospora crassa ro-10 and ro-11 genes encode novel proteins required for nuclear distribution. Mol Microbiol 32, 1065-1076.
Mirdita, M., Schutze, K., Moriwaki, Y., Heo, L., Ovchinnikov, S., and Steinegger, M. (2022). ColabFold: making protein folding accessible to all. Nat Methods 19, 679-682.
Moon, H.M., Youn, Y.H., Pemble, H., Yingling, J., Wittmann, T., and Wynshaw-Boris, A. (2014). LIS1 controls mitosis and mitotic spindle organization via the LIS1-NDEL1-dynein complex. Hum Mol Genet 23, 449-466.
Moore, J.K., Li, J., and Cooper, J.A. (2008). Dynactin function in mitotic spindle positioning. Traffic 9, 510-527.
Morgan, J.L., Song, Y., and Barbar, E. (2011). Structural dynamics and multiregion interactions in dynein-dynactin recognition. J Biol Chem 286, 39349-39359.
Morgan, J.L., Yeager, A., Estelle, A.B., Gsponer, J., and Barbar, E. (2021). Transient Tertiary Structures of Disordered Dynein Intermediate Chain Regulate its Interactions with Multiple Partners. J Mol Biol 433, 167152.
Myers, K.R., Lo, K.W., Lye, R.J., Kogoy, J.M., Soura, V., Hafezparast, M., and Pfister, K.K. (2007). Intermediate chain subunit as a probe for cytoplasmic dynein function: biochemical analyses and live cell imaging in PC12 cells. J Neurosci Res 85, 2640-2647.
Nyarko, A., Song, Y., and Barbar, E. (2012). Intrinsic disorder in dynein intermediate chain modulates its interactions with NudE and dynactin. J Biol Chem 287, 24884-24893.
Pettersen, E.F., Goddard, T.D., Huang, C.C., Meng, E.C., Couch, G.S., Croll, T.I., Morris, J.H., and Ferrin, T.E. (2021). UCSF ChimeraX: Structure visualization for researchers, educators, and developers. Protein Sci 30, 70-82.
Poirier, K., Lebrun, N., Broix, L., Tian, G., Saillour, Y., Boscheron, C., Parrini, E., Valence, S., Pierre, B.S., Oger, M., et al. (2013). Mutations in TUBG1, DYNC1H1, KIF5C and KIF2A cause malformations of cortical development and microcephaly. Nat Genet 45, 639-647.
Qiu, R., Zhang, J., and Xiang, X. (2019). LIS1 regulates cargo-adapter-mediated activation of dynein by overcoming its autoinhibition in vivo. J Cell Biol 218, 3630-3646.
Quintyne, N.J., Gill, S.R., Eckley, D.M., Crego, C.L., Compton, D.A., and Schroer, T.A. (1999). Dynactin is required for microtubule anchoring at centrosomes. J Cell Biol 147, 321-334.
Raaijmakers, J.A., Tanenbaum, M.E., and Medema, R.H. (2013). Systematic dissection of dynein regulators in mitosis. J Cell Biol 201, 201-215.
Rao, L., Romes, E.M., Nicholas, M.P., Brenner, S., Tripathy, A., Gennerich, A., and Slep, K.C. (2013). The yeast dynein Dyn2-Pac11 complex is a dynein dimerization/processivity factor: structural and single-molecule characterization. Mol Biol Cell 24, 2362-2377.
Reck-Peterson, S.L., Redwine, W.B., Vale, R.D., and Carter, A.P. (2018). The cytoplasmic dynein transport machinery and its many cargoes. Nat Rev Mol Cell Biol 19, 382-398.
Reck-Peterson, S.L., Yildiz, A., Carter, A.P., Gennerich, A., Zhang, N., and Vale, R.D. (2006). Single-molecule analysis of Dynein processivity and stepping behavior. Cell 126, 335-348.
Roossien, D.H., Lamoureux, P., and Miller, K.E. (2014). Cytoplasmic dynein pushes the cytoskeletal meshwork forward during axonal elongation. J Cell Sci 127, 3593-3602.
Saito, K., Murayama, T., Hata, T., Kobayashi, T., Shibata, K., Kazuno, S., Fujimura, T., Sakurai, T., and Toyoshima, Y.Y. (2020). Conformational diversity of dynactin sidearm and domain organization of its subunit p150. Mol Biol Cell 31, 1218-1231.
Sasaki, S., Shionoya, A., Ishida, M., Gambello, M.J., Yingling, J., Wynshaw-Boris, A., and Hirotsune, S. (2000). A LIS1/NUDEL/cytoplasmic dynein heavy chain complex in the developing and adult nervous system. Neuron 28, 681-696.
Schlager, M.A., Hoang, H.T., Urnavicius, L., Bullock, S.L., and Carter, A.P. (2014). In vitro reconstitution of a highly processive recombinant human dynein complex. Embo J 33, 1855-1868.
Scoto, M., Rossor, A.M., Harms, M.B., Cirak, S., Calissano, M., Robb, S., Manzur, A.Y., Martinez Arroyo, A., Rodriguez Sanz, A., Mansour, S., et al. (2015). Novel mutations expand the clinical spectrum of DYNC1H1-associated spinal muscular atrophy. Neurology 84, 668-679.
Sheeman, B., Carvalho, P., Sagot, I., Geiser, J., Kho, D., Hoyt, M.A., and Pellman, D. (2003). Determinants of S. cerevisiae dynein localization and activation: implications for the mechanism of spindle positioning. Curr Biol 13, 364-372.
Siglin, A.E., Sun, S., Moore, J.K., Tan, S., Poenie, M., Lear, J.D., Polenova, T., Cooper, J.A., and Williams, J.C. (2013). Dynein and dynactin leverage their bivalent character to form a high-affinity interaction. PLoS One 8, e59453.
Splinter, D., Razafsky, D.S., Schlager, M.A., Serra-Marques, A., Grigoriev, I., Demmers, J., Keijzer, N., Jiang, K., Poser, I., Hyman, A.A., et al. (2012). BICD2, dynactin, and LIS1 cooperate in regulating dynein recruitment to cellular structures. Mol Biol Cell 23, 4226-4241.
Tan, R., Lam, A.J., Tan, T., Han, J., Nowakowski, D.W., Vershinin, M., Simo, S., Ori-McKenney, K.M., and McKenney, R.J. (2019). Microtubules gate tau condensation to spatially regulate microtubule functions. Nat Cell Biol 21, 1078-1085.
Tarricone, C., Perrina, F., Monzani, S., Massimiliano, L., Kim, M.H., Derewenda, Z.S., Knapp, S., Tsai, L.H., and Musacchio, A. (2004). Coupling PAF signaling to dynein regulation: structure of LIS1 in complex with PAF-acetylhydrolase. Neuron 44, 809-821.
Ton, W.D., Wang, Y., Chai, P., Beauchamp-Perez, C., Flint, N.T., Lammers, L.G., Xiong, H., Zhang, K., and Markus, S.M. (2022). Microtubule binding-induced allostery promotes LIS1 dissociation from dynein prior to cargo transport. bioRxiv, 2022.2011.2008.515461.
Toropova, K., Zou, S., Roberts, A.J., Redwine, W.B., Goodman, B.S., Reck-Peterson, S.L., and Leschziner, A.E. (2014). Lis1 regulates dynein by sterically blocking its mechanochemical cycle. eLife 3.
Tripathy, S.K., Weil, S.J., Chen, C., Anand, P., Vallee, R.B., and Gross, S.P. (2014). Autoregulatory mechanism for dynactin control of processive and diffusive dynein transport. Nat Cell Biol 16, 1192-1201.
Trokter, M., Mucke, N., and Surrey, T. (2012). Reconstitution of the human cytoplasmic dynein complex. Proc Natl Acad Sci U S A 109, 20895-20900.
Urnavicius, L., Lau, C.K., Elshenawy, M.M., Morales-Rios, E., Motz, C., Yildiz, A., and Carter, A.P. (2018). Cryo-EM shows how dynactin

recruits two dyneins for faster movement. Nature 554, 202-206.
Urnavicius, L., Zhang, K., Diamant, A.G., Motz, C., Schlager, M.A., Yu, M., Patel, N.A., Robinson, C.V., and Carter, A.P. (2015). The structure of the dynactin complex and its interaction with dynein. Science 347, 1441-1446.
Vaughan, K.T., and Vallee, R.B. (1995). Cytoplasmic dynein binds dynactin through a direct interaction between the intermediate chains and p150 ^{Glued}. J Cell Biol 131, 1507-1516.
Wang, S., Ketcham, S.A., Schon, A., Goodman, B., Wang, Y., Yates, J., 3rd, Freire, E., Schroer, T.A., and Zheng, Y. (2013). Nudel/NudE and Lis1 promote dynein and dynactin interaction in the context of spindle morphogenesis. Mol Biol Cell 24, 3522-3533.
Wang, S., and Zheng, Y. (2011). Identification of a novel dynein binding domain in nudel essential for spindle pole organization in Xenopus egg extract. J Biol Chem 286, 587-593.
Willemsen, M.H., Vissers, L.E., Willemsen, M.A., van Bon, B.W., Kroes, T., de Ligt, J., de Vries, B.B., Schoots, J., Lugtenberg, D., Hamel, B.C., et al. (2012). Mutations in DYNC1H1 cause severe intellectual disability with neuronal migration defects. J Med Genet 49, 179-183.
Yi, J.Y., Ori-McKenney, K.M., McKenney, R.J., Vershinin, M., Gross, S.P., and Vallee, R.B. (2011). High-resolution imaging reveals indirect coordination of opposite motors and a role for LIS1 in high-load axonal transport. J Cell Biol 195, 193-201.
Zaw Min Htet, J.P.G., Richard W. Baker, Andres E. Leschziner, Morgen E. DeSantis, Samara L. Reck-Peterson (2020). LIS1 Promotes the Formation of Activated Cytoplasmic Dynein-1 Complexes. Nature cell biology.
Zhang, K., Foster, H.E., Rondelet, A., Lacey, S.E., Bahi-Buisson, N., Bird, A.W., and Carter, A.P. (2017). Cryo-EM Reveals How Human Cytoplasmic Dynein Is Auto-inhibited and Activated. Cell 169, 1303-1314 e1318.
Zhang, Q., Wang, F., Cao, J., Shen, Y., Huang, Q., Bao, L., and Zhu, X. (2009). Nudel promotes axonal lysosome clearance and endo-lysosome formation via dynein-mediated transport. Traffic 10, 1337-1349.
Zylkiewicz, E., Kijanska, M., Choi, W.C., Derewenda, U., Derewenda, Z.S., and Stukenberg, P.T. (2011). The N-terminal coiled-coil of Ndel1 is a regulated scaffold that recruits LIS1 to dynein. J Cell Biol 192, 433-445.

Acknowledgements

We are grateful to members of the McKenney, Ori-McKenney, Markus, DeLuca, and DeSantis labs for valuable discussions. Electron microscopy was done at the University of Colorado, Boulder EM Services Core Facility in the MCDB Department, with the technical assistance of facility staff, or in the Biological Electron Microscopy Facility at UC Davis. This work utilized the RMACC Summit supercomputer, which is supported by the National Science Foundation (awards ACI-1532235 and ACI-1532236), the University of Colorado Boulder and Colorado State University. The RMACC Summit supercomputer is a joint effort of the University of Colorado Boulder and Colorado State University. This work was funded by the NIH/NIGMS (2R35GM124889 and 4R00NS089428 to R.J.M, and R35GM139483 to S.M.M.). This paper was typeset with the bioRxiv word template by @Chrelli: www.github.com/chrelli/bioRxiv-word-template

Author contributions

R.J.M and S.M.M. designed the study, acquired funding, generated figures, and wrote and edited the manuscript. KO and BI generated reagents, performed experiments, analyzed the in-cell, *in vivo*, and *in vitro* data, helped prepare figures, and edited the manuscript. LL performed and analyzed the spindle oscillation experiments. WL and PG generated reagents for work with metazoan proteins and performed initial TIRF experiments. All authors edited the paper.

Competing interest statement

The authors have no competing interests to declare.

Materials and Methods

Media and strain construction

Yeast strains are derived from W303 or YEF473A (Bi and Pringle, 1996) and are available upon request. We transformed yeast strains using the lithium acetate method (Knop et al., 1999) Strains carrying mutations or tagged components were constructed by PCR product-mediated transformation (Longtine et al., 1998) or by mating followed by tetrad dissection. Proper tagging and mutagenesis were confirmed by PCR, and in some cases sequencing. Fluorescent tubulin-expressing yeast strains were generated using plasmids and strategies described previously (Markus et al., 2015) Strains overexpressing the yeast dynein complex (WT or ΔICN) were generated by transforming p8His-ZZ-SNAPf-Dynein or p8His-ZZ-HALO-Dynein (wild-type or mutants; see below) linearized by digestion with ApaI. Strains overexpressing yeast Ndl1 or Pac1 were generated by transforming pRS306:GAL1p:Ndl1-FLAG-SNAPf-TEV-ZZ-8xHis, or pRS306:GAL1p:8xHIS-ZZ-2xTEV-Pac1-FLAG-SNAPf (wild-type or mutants) linearized by digestion with ApaI. Integration was confirmed by diagnostic PCR. Yeast synthetic defined (SD) medium was obtained from Sunrise Science Products. (San Diego, CA).

Plasmid construction

Rat IC2C (Uniprot ID:Q13409) WT and ΔICN with C-terminal SNAP-FLAG-strepII tag were cloned into pcDNA5-FRT-TO. Full-length human Ndel1 (Uniprot ID: Q9GZM8, or the coiled-coil domain, Ndel1^{CC}, residues 1-195) were cloned into pET28a with StrepII-sfGFP-PPS tags at its N-terminus, and FLAG tag at its C-terminus. Mutations in NudEL were generated by site-directed mutagenesis using hotstart Q5 DNA polymerase (New England Biolab). Human dynactin p150-CC1 (Uniprot ID: Q14203, residues 224-554) was cloned into pET28a with N-terminal StrepII-SNAPf-PPS tags. The N-terminal coiled-coil domain of mouse BicD2 (residues 25-425) and the SNAPf-tagged and GST-dimerized human dynein motor domain were previously described (McKenney et al., 2014). SNAPf-tagged and 6xhis-tagged LIS1 expression constructs were previously described (Gutierrez et al., 2017). A plasmid encoding the entire yeast dynein complex (Marzo. et al., 2020)was used to generate the ΔICN mutant (with N-terminal 43 residues of Pac11 deleted). Full-length yeast Ndl1 with C-terminal FLAG-SNAPf-TEV-ZZ-8xHis tags was cloned into pRS306. The Ndl1 coiled-coil domain (residues 2-132) with N-terminal 6xHis-StrepII-sfGFP tags was cloned into pET28a. The Nip100 coiled-coil (residues 97-377) were cloned into a pGEX-KG vector such that the Nip100^{CC1} possessed an N-terminal SUMO-eGFP tag. Full-length yeast Pac1 with N-terminal 8xHIS-ZZ-2xTEV tags, and C-terminal FLAG-SNAPf tags was cloned into pRS306. All plasmids (and mutations as indicated throughout) were generated using Gibson assembly and the coding sequences were validated by DNA sequencing.

Generation of IC2C Flp-In T-REx 293 cell lines and large scale expression

Flp-In™ T-REx™293 cells (Thermo Fisher) harboring IC2C wt or ΔICN with C-terminal SNAP-FLAG-strepII tagwhich were generated using the FLP/FRT system (Thermo Fisher). Briefly, pcDNA5-FRT-TOconstruct and pOG44, which expresses Flipase, were co-transfected using Lipofectamine 2000 (Thermo Fisher) into Flp-In™ T-REx™293 cells (Thermo Fisher). After recovery from transfection, cells were grown in DMEM containing 10% FBS, 1% Penicillin-Streptomycin, and 100 μg/mL Hygromycin B to select cells in which pcDNA5 construct was inserted into FRT locus. The expression of tagged IC2C was verified by western blotting with antibodies against StrepII tag (Novus Biologicals). These cell lines were grown in culture vessels (Corning, Fisher Scientific) to 80% confluence, and then tagged IC2C expression was induced with 1 μg/ml doxycycline for two days. Cells were harvested in PBS by tapping the culture vessels, and spun down at 1200 rpm for 5 min in Sorvall Legend XTR. Cell pellets were washed with PBS, snap frozen in liquid nitrogen, and stored at -80ºC.

Protein purification

Porcine brain tubulin was isolated using the high-molarity PIPES procedure as described (Castoldi and Popov, 2003) and then labeled with biotin- or Dylight-405 NHS-ester (Invitrogen) as described

(http://mitchison.hms.harvard.edu/files/mitchisonlab/files/labeling_tubulin_and_quantifying_labeling_stoichiometry.pdf). Microtubules were prepared by incubating tubulin with 1 mM GTP for 10 min at 37 °C, followed by diluting into 20 μM taxol and continuing incubation for an additional 20 min. Microtubules were pelleted through 25% sucrose cushion with 10 μM taxol at 80,000 rpm in a TLA-100 rotor, and the pellet was resuspended in BRB80 containing 10 μM taxol. Human dynein complexes were purified from Flp-In T-Rex cell pellet prepared as above. Cells were lysed in lysis buffer (50 mM Tris-HCl, pH 8.0, 150 mM KCH_3COO, 2 mM $MgSO_4$, 1 mM EGTA, 10% glycerol) supplemented with 0.2% Triton X-100, 0. 1mM ATP, 1 mM DTT, 1 mM PMSF, and DNaseI. Cell lysate was clarified at 147,000 x g for 15 min at 4ºC in Beckman MLA-50 rotor. The resulting supernatant was passed through HiPrep26/10 desalting column to remove free biotin, then loaded onto a column packed with strep-tactin XT 4Flow resin (Iba Lifesciences GmbH). The column was washed with 5 column volume of lysis buffer containing 250 mM NaCl followed by 10 column volume of lysis buffer. Proteins were eluted with 50 mM biotin, concentrated with an Amicon-Ultra MWCO 100kDa filter, and then gel filtered on a Yarra 3μm SEC-4000 LC column 300 x 21.2 mm (Phenomenex) equilibrated with GF150 buffer (25 mM HEPES-KOH, 150 mM KCl, 2 mM $MgCl_2$). Peak fractions containing intact dynein were supplemented with 0.1 mM ATP, 1 mM DTT and 10% glycerol, and concentrated before being snap-frozen in liquid nitrogen, and stored at -80°C. For labeling purified proteins with SNAP dyes, proteins were incubated with 2–5 molar excess of SNAP dye (SNAP- Alexa 647, SNAP-TMR star or SNAP-Surface 488) for 1 h on ice. The unbound dye was removed using HiTrap desalting columns (Thermo Fisher). The stoichiometry of labeling was assessed using a Nanodrop One (Thermo Fisher) and comparing the absorbance of total protein at 280 nm to the absorbance at the SNAP- dye wavelength.

Porcine brain dynactin was purified according to (Zhang et al., 2017). Purified BicD2 and Hook3 1-552 were used to isolate DDA complexes from rat brain cytosol as previously described (McKenney et al., 2014). DDA complexes were labeled with 5 μM SNAP-TMR dye during the isolation procedure, snap-frozen in small aliquots, and stored at -80 °C. StrepII-SNAPf-LIS1 and 6xhis-LIS1 were expressed in Sf9 cells and purified as described before (Gutierrez et al., 2017). Bacteria expression constructs for BicD2, Hook3 1-552, NudEL-FL, NudEL-CC, and p150-CC1 were transformed into BL21-CodonPlus (DE3)-RIPL (Agilent) and the bacteria were grown in LB medium at 37 ºC until OD_{600} reaches to 0.6. The protein expression was induced with 0.2 mM isopropyl-β-D-thiogalactoside overnight at 18°C, except the p150-CC1 construct which was induced for 2 hours at 37ºC. Cells were harvested and resuspended in lysis buffer supplemented with 1 mM DTT, 1 mM PMSF, DNaseI. Cells were lysed by passing through an Emulsiflex C3 high-pressure homogenizer (Avestin). Then the lysates were centrifuged at 15,000 x g for 20 min at 4°C and the supernatant was passed over a column packed with Strep-tactin XT 4Flow resin (Iba Lifesciences GmbH). The column was washed with lysis buffer, and bound proteins were eluted in lysis buffer containing 50 mM biotin (Chem-Impex International). For StrepII-sfGFP cleaved NudEL-FL and NudEL-CC used in Figure 5E and F , the proteins were cleaved while bound to the columns with Prescission protease, and cleaved NudEL-FL and NudEL-CC were collected. Eluted proteins were directly loaded onto HiTrap Q HP column (GE Healthcare) and eluted with 0-0.6M NaCl gradient. Peak fractions were concentrated on Amicon-Ultra filters and passed through an EnRich650 (Bio-Rad) or Superpose 6 10/300 GL (GE Healthcare) size exclusion column, in lysis buffer. Peak fractions were collected, concentrated again, and frozen after supplemented with 1mM DTT and 10% glycerol.

Purification of the yeast dynein complex (6xHis-ZZ-TEV-HALO-or SNAPf-Dynein, with all genes, including Dyn2, Dyn3 and Pac11 under the control of the GAL1p promoter) was performed as previously described with minor modifications (Marzo. et al., 2020). In brief, yeast cultures were grown in YPA medium supplemented with 2% galactose for no more than 3 hours, collected, washed with cold water and then resuspended in a small volume of water. The resuspended cell pellet was drop-frozen into liquid nitrogen and then lysed in a coffee grinder. After lysis, 0.25 volumes of 4X dynein lysis buffer (1X buffer: 30 mM HEPES-KOH pH 7.2, 50 mM potassium acetate, 2 mM magnesium acetate, 0.2 mM EGTA) supplemented with 1 mM dithiothreitol (DTT), 0.1 mM Mg-ATP and 0.5 mM Pefabloc SC or protease inhibitor tablets (Pierce) (concentrations for the 1X buffer) was added, and the lysate was clarified by centrifugation at 310,000 x g for 1 hour. The supernatant was then incubated with IgG sepharose 6 fast flow resin (GE) for 1-2 hours at 4°C, which was subsequently washed three times in 5 ml lysis buffer, and twice in 5 ml TEV buffer (50 mM Tris-HCl pH 8.0, 150 mM potassium acetate, 2 mM magnesium acetate, 1 mM EGTA and 10% glycerol) supplemented with 0.005% Triton X-100, 1 mM DTT, 0.1 mM Mg-ATP and 0.5 mM Pefabloc SC. To fluorescently label the dyneins, the bead-bound protein was incubated with 5-10 μM JF503-HaloTag, JFX549-HaloTag, or JFX646-HaloTag ligand (Janelia Research Campus), as appropriate, for 10-20 min at room temperature. The resin was then washed four more times in TEV buffer supplemented with 1 mM DTT, 0.005% Triton X-100 and 0.1 mM Mg-ATP, and then incubated with TEV protease for 1-1.5 h at 16 °C. After digestion with TEV, the beads were pelleted, and the resulting supernatant was collected, aliquoted, flash-frozen in liquid nitrogen, and stored at -80 °C. Protein preparations used for negative stain EM imaging (6xHis-ZZ-TEV-SNAPf-Dynein) were tandem-affinity purified. To do so, subsequent to lysis, 0.25 volumes of 4X NiNTA dynein lysis buffer (1X buffer: 30 mM HEPES pH 7.2, 200 mM potassium acetate, 2 mM magnesium acetate and 10% glycerol) supplemented with 1 mM beta-mercaptoethanol, 0.1 mM Mg-ATP and 0.5 mM Pefabloc SC (concentrations for the 1X buffer) was added, and the lysate was clarified as described above. The supernatant was then bound to NiNTA agarose for 1 h at 4°C, which was subsequently washed three times in 5 ml NiNTA lysis buffer. The protein was eluted in NiNTA lysis buffer supplemented with 250 mM imidazole by incubation for 10 min on ice. The eluate was then diluted with an equal volume of dynein lysis buffer, which was then incubated with IgG Sepharose 6 fast flow resin for 1 h at 4°C. The beads were washed and the protein was eluted as described above (with TEV protease). Eluted protein was either applied to a size-exclusion resin (Superose 6; GE) or snap-frozen. The gel filtration resin was equilibrated in GF150 buffer (25 mM HEPES-KOH pH 7.4, 150 mM KCl, 1 mM $MgCl_2$, 5 mM DTT and 0.1 mM Mg-ATP) using an AKTA Pure system. Peak fractions (determined by absorbance at 260 nm and SDS–PAGE) were pooled, concentrated, aliquoted, flash-frozen and then stored at −80 °C.

Purification of Ndl1-SNAPf-TEV-ZZ was performed using the same procedure as that for ZZ-TEV-Pac1-SNAPf as previously described (Marzo. et al., 2020), with the addition of a gel filtration step to remove residual, unbound fluorescent dye. Specifically, proteins were fluorescently labeled by incubating the bead-bound protein with either 10 μM JFX554-SNAPTag or JFX650-SNAP-tag ligand (Janelia Research Campus), as appropriate, for 1 hour at 4°C. The resin was then washed four times in TEV buffer supplemented with 0.005% Triton X-100, 1 mM DTT and 0.5 mM Pefabloc SC, then incubated in TEV buffer supplemented with TEV protease overnight at 4°C. Following TEV digest, the supernatant was collected using a spin filtration device, and applied to a size exclusion chromatography resin (Superose 6; GE) that was equilibrated in TEV buffer supplemented with 1 mM DTT using an AKTA Pure. Peak fractions (determined by absorbance at 260 nm and SDS-PAGE) were pooled, concentrated, aliquoted, flash-frozen and then stored at -80°C.

To purify StrepII-sfGFP-Ndl1^{CC} (residues 2-132), cultures of BL21-CodonPlus (DE3)-RIPL containing the plasmid were grown at 37°C until O.D.~0.8 at which point protein expression was induced with 1 mM IPTG, and the temperature was shifted to 16°C. After an overnight incubation, cells were harvested, washed with water, and frozen. Cell pellets were resuspended in lysis buffer W (100 mM Tris-HCl, pH 8.0, 150 mM NaCl, 1 mM EDTA) by passage through a microfluidizer three times at 18,000 psi. The cell lysate was clarified by centrifugation at 23,000 x g for 20 min, and the clarified lysate was then loaded onto a gravity flow column packed with Strep-tactin XT agarose beads (Iba Lifesciences). After binding, the column was washed extensively, and the bound protein was eluted in lysis buffer W supplemented with 50 mM biotin. After elution, peak fractions were concentrated, and gel filtered using a Superdex 200 16/60 gel filtration column (GE Healthcare). The peak fractions were concentrated, flash frozen, and then stored at -80°C.

To purify GST-eGFP-Nip100^{CC1} (residues 97-377), cultures of BL21-CodonPlus (DE3)-RIPL containing the plasmid were grown and harvested as described above. Cell pellets were resuspended in lysis buffer W by passage through a microfluidizer three times at 18,000 psi. The cell lysate was clarified by centrifugation at 310,000 x g for 1 hour. The supernatant

was incubated with Glutathione agarose 4 resin for 1-2 hours at 4°C, which was subsequently washed three times in 5 ml buffer W. The protein-containing resin was then incubated with Ulp1 protease for 1-1.5 h at 16 °C. Following Ulp1 digest, the supernatant was collected using a spin filtration device, and gel filtered using a Superdex 200 16/60 gel filtration column (GE Healthcare). The peak fractions were concentrated, flash frozen, and then stored at -80°C.

Single and ensemble molecule motility assays

The single-molecule motility assays with yeast proteins were performed using previously reported protocols (Chandradoss et al., 2014; Markus et al., 2012)with minor modifications. Briefly, coverslips were cleaned with acetone and potassium hydroxide, followed by oxygen plasma treatment (for 10 minutes). The coverslips were silanized with 3-aminopropyl trimethoxysilane (APTES), and then coated with a biotinylated polyethylene glycol (PEG) solution (a mixture of methoxyPEG-succinimidyl valerate and biotin-PEG-succinimidyl valerate dissolved in a freshly prepared solution of 0.1 M sodium bicarbonate). The coverslips were adhered to glass slides using double-sided adhesive tape, thereby producing narrow chambers (~4-7 µl in volume). The flow chambers were incubated with streptavidin (0.1 mg/ml), and then blocked with 1% Pluronic F-127. Taxol-stabilized, biotinylated microtubules assembled from unlabeled and biotin-labeled porcine tubulin (4:1 ratio) were introduced into the chamber. Following a 5-10 minute incubation, the chamber was washed with dynein lysis buffer supplemented with 20 µM taxol, after which dynein diluted in an oxygen-scavenging motility buffer (30 mM HEPES, pH 7.2, 50 mM potassium acetate, 2 mM magnesium acetate, 1 mM EGTA, 10% glycerol, 50 nM protocatechuate 3,4-dioxygenase, 2.5mM protocatechuic acid, 1 mM Trolox, 1 mM cyclooctatetraene, 1 mM 4-nitrobenzyoyl alcohol) supplemented with 1 mM DTT, 20 µM taxol, and 1 mM Mg-ATP was added. TIRFM images were immediately collected using a 1.49 NA 100X TIRF objective on a Nikon Ti-E inverted microscope equipped with a Ti-S-E motorized stage, piezo Z-control (Physik Instrumente), and an iXon X3 DU897 cooled EM-CCD camera (Andor). 488 nm, 532 nm, and 640 nm lasers were used along with a multi-pass quad filter cube set (C-TIRF for 405/488/561/638 nm; Chroma) and emission filters mounted in a filter wheel (525/50 nm, 600/50 nm and 700/75 nm; Chroma). We acquired images at 1 second intervals for 8 min. Velocity and run length values were determined from kymographs generated using the MultipleKymograph plugin for ImageJ (http://www.embl.de/eamnet/html/body_kymograph.html). Mean run length values for individual runs were determined by fitting the cumulative distribution functions to a one-phase decay in GraphPad Prism, as previously described (Ecklund et al., 2017; Marzo. et al., 2020).

Single molecule assays with mammalian proteins were performed in chambers with surface adhered porcine microtubules essentially as previously described (Lam et al., 2021; Tan et al., 2019). The buffer used for these assays was SRP90 (90 mM HEPES-KOH pH7.4, 50 mM K- acetate, 2 mM Mg-acetate, 1 mM EGTA, 10% glycerol supplemented with 0.5 % Pluronic F-127, 0.1 mg/ml biotin-BSA, 0.2 mg/ml BSA, 0.2 mg/ml κ-casein, 10 µM Taxol, 2 mM Trolox, 2mM protocatechuic acid, 50 nM protocatechuate-3,4-dioxygenase, 2mM Mg-ATP) .

For microtubule gliding assays, 0.5 µM human dynein was flowed into empty chambers. After incubating the chamber for 5 min, unbound proteins were washed away with SRP90 assay buffer. Dylight-405-labeled microtubules diluted in assay buffer were flowed in, and images were acquired every 5 seconds. Kymographs of microtubules were prepared using ImageJ software, and velocities were determined based on translocation over time. For DDH single molecule motility assays, 30 nM DDH and indicated concentrations of either p150-CC1 or Ndel1 in the SRP90 assay buffer were flowed into the glass chamber. Images were acquired every 0.5 sec for 2 min. All images were acquired using a Nikon TE microscope (1.493NA, 100X objective) equipped with a TIRF illuminator and Andor iXon CCD EM camera.

Microtubule recruitment assays

For yeast proteins, flow chambers constructed using slides and plasma cleaned and silanized coverslips attached with double-sided adhesive tape were coated with anti-tubulin antibody (8 mg/ml, YL1/2; Accurate Chemical & Scientific Corporation) then blocked with 1% Pluronic F-127 (Fisher Scientific). Taxol-stabilized microtubules assembled from unlabeled porcine tubulin (Cytoskeleton) were introduced into the chamber. After microtubules were adhered to the cover glass, the chambers were washed with TEV buffer supplemented with 1 mM DTT and 20 µM taxol. Following this, mixtures of purified proteins (e.g., dynein ± Ndl1; as described throughout the text and in figure legends) were flowed into the chambers, after which the chambers were incubated for 5-10 minutes and then imaged. Quantitation was performed using ImageJ /FIJI software (National Institutes of Health). Fluorescence intensities in each channel were measured along microtubules ("signal"), and adjacent to microtubules ("background"). Mean corrected pixel intensity was determined by subtracting background from signal.

Assays with mammalian proteins were carried out as follows: a mixture of unlabeled tubulin, biotin-tubulin, and DyLight405-labeled microtubules were prepared as described. Microtubules were pelleted over a 25% sucrose cushion in BRB80 buffer to remove unpolymerized tubulin. TIRF chambers were assembled from acid-washed coverslips and double-sided sticky tape. Chambers were first incubated with 0.5 mg/ml PLL-PEG-Biotin (Surface Solutions) for 10 min, followed by 0.5 mg/ml streptavidin for 5 min. MTs diluted into taxol containing BRB80 buffer were then incubated in the chamber and allowed to adhere to the streptavidin-coated surface. Unbound MTs were washed away with SRP90 assay buffer. Proteins (e.g., dynein, LIS1, Ndel1) were diluted in assay buffer at concentrations indicated in Figure legends supplemented with 2 mM AMP-PNP (Roche). Prior to image acquisition, chambers were incubated 10 min to allow proteins to reach steady-state.

Live cell imaging experiments

For the single time point spindle position assay, the percentage of cells with a misoriented anaphase spindle was determined after growth overnight (12-16 hours) at a low temperature (16°C), as previously described (Li et al., 2005; Markus et al., 2009; Sheeman et al., 2003). A single z-stack of wide-field fluorescence images was acquired for mTurquoise2- or mRuby2-Tub1, as appropriate. For the spindle oscillation assay (Ecklund et al., 2023), cells were arrested with 200 mM hydroxyurea (HU) for 2.5 hours, and then mounted on agarose pads containing HU for fluorescence microscopy. GFP-labeled microtubules (GFP-Tub1) were imaged every 10 seconds for 10 minutes. To image dynein localization, cells were grown in synthetic defined (SD) media supplemented with either glucose, raffinose, or raffinose plus galactose (for GAL1p experiments; induced for 3.5 hours), and mounted on agarose pads. Images were collected on a Nikon Ti-E microscope equipped with a 1.49 NA 100X TIRF objective, a Ti-S-E motorized stage, piezo Z-control (Physik Instrumente), an iXon DU897 cooled EM-CCD camera (Andor) with an emission filter wheel (ET480/40M for mTurquoise2, ET525/50M for GFP, ET520/40M for YFP, and ET632/60M for mRuby2; Chroma). The microscope was controlled with NIS Elements software (Nikon). Image analysis was performed using ImageJ/FIJI software (National Institutes of Health). Plus end, cortical, and SPB foci were identified in two-color movies and scored accordingly. Specifically, plus end molecules were recognized as those foci that localized to the distal tips of dynamic microtubules (identified via mTurquoise2- or mRuby2-Tub1 imaging), whereas spindle pole body (SPB)-associated molecules were recognized as those foci that localized to one of the spindle poles. Cortical molecules were identified as those foci not associated with an astral microtubule plus end that remained stationary at the cell cortex for at least three frames.

Mitotic index measurement

T-Rex Flp-In 293 cells were grown on coverslips, and DIC (WT or ΔICN) expression was induced with 1 µg/ml doxycycline for 2 days. Cells (~60% confluent) were fixed with 4% paraformaldehyde for 15 min, rinsed with PBS, and permeabilized subsequently with 0.1% Triton-X100/PBS. Cells were stained with anti-tubulin antibody DM1A (Cell Signaling), anti-SNAP tag (Invitrogen), and DAPI. Cell images were collected from 5 randomly selected fields and mitotic cells were scored.

Mass Photometry

To prepare chambers, high precision microscope coverslips (No. 1.5, 24 × 50, cat# 0107222, Marienfeld, Lauda-K önigshofen, Germany) were cleaned by sequential sonication in ultrapure H_2O (10 min), isopropanol (10 min), then ultrapure H_2O, and dried with filtered air. Culturewell™ gaskets (3

mm diam x 1 mm depth, cat#103250, Grace Bio-Labs, Bend, OR) were cut and rinsed with isopropanol and ultrapure H_2O, then dried with filtered air and placed onto the freshly cleaned cover glasses. To focus, 15µl buffer (90 mM HEPES-KOH pH7.4, 50 mM K- acetate, 2 mM Mg-acetate, 1 mM EGTA, 10% glycerol supplemented) was first applied to the well, and the focal position was identified and secured in place with an autofocus system based on total internal reflection for the entire measurement period. Immediately before mass photometry measurements, protein stocks were diluted in the same buffer and 5 µl of diluted protein (5-20nM final concentration) was added into the well. All data were acquired using an OneMP mass photometer (Refeyn Ltd, Oxford, UK) at the rate of 1 kHz for 60 s by AcquireMP (Refeyn Ltd). Each sample was measured at least three times independently. Calibration standard was generated using BSA (Sigma), Alcohol dehydrogenase (A7011, Sigma) and beta-amylase (A8781, Sigma). Data analysis was performed using DiscoverMP (Refeyn Ltd).

Mass photometry data with yeast proteins (Pac1 and Ndl1-CC) were performed similarly, but with a TwoMP mass photometer (Refeyn Ltd, Oxford, UK). All proteins were initially diluted to 150 nM in assay buffer (50 mM Tris, pH 8.0, 150 mM potassium acetate, 2 mM magnesium acetate, 1 mM EGTA, 1 mM DTT). 2 µl of each was then mixed 1:1 (to 75 nM of each), incubated for 1-2 minutes, and then diluted 1:5 on the stage (2.5 µl of mixed protein + 10 µl assay buffer) to 15 nM final immediately prior to image acquisition. For individual measurements, protein was diluted 1:10 on the stage (1.5 µl of protein + 13.5 µl assay buffer). 1 minute movies were acquired using AcquireMP, and all images were processed and analyzed using DiscoverMP.

Negative stain EM and image analysis

EM grids were prepared by applying fresh dynein samples (WT or ΔICN, after tandem affinity purification; see above) to glow-discharged carbon-coated 200 mesh copper grids. After incubation for ~1 min, 2% uranyl acetate was added. Micrographs were collected with a FEI Tecnai F20 200 kV TEM equipped with a Gatan US4000 CCD (model 984), at a nominal magnification of X90,000 with a digital pixel size of 6.19 Å. All image analysis was performed using Relion v.3.0 on the University of Colorado Boulder High Performance Computer Cluster, Summit. Particles were manually picked from ~20 micrographs (~200 particles), which were used to generate a low-resolution 2D class average. Using these 2D averages as a starting point, we then used an iterative process to autopick particles that were used to generate our final 2D averages.

AlphaFold predictions

Although a crystal structure of the coiled-coil domain of Ndel1 revealed a tetramer (Derewenda et al., 2007), we chose to model these molecules as dimers in light of our mass photometry data. For our models with Pac1 or LIS1, we used a stoichiometry of 1 Ndel1/Ndl1 dimer to 1 LIS1/Pac1 dimer, which was also guided by our mass photometry data. Finally, for our Ndel1/Ndl1-ICN complexes – which were modeled without LIS1/Pac1 – we chose to use a stoichiometry of 1 Ndel1/Ndl1 to 2 ICNs given the small size of these fragments, and the likely presence of two ICN-binding sites within a Ndel1/Ndl1 dimer. Models were generated using ColabFold running on Google Colaboratory (Mirdita et al., 2022), and images were manipulated and prepared using ChimeraX (Pettersen et al., 2021).

Statistical analyses

All data were collected from at least two independent replicates (independent protein preparations or cell cultures for in vitro and in vivo experiments, respectively). The values from each independent replicate – which are indicated on each plot – showed similar results. For all datasets, P-values were calculated from Z scores (when comparing proportions) as previously described (Marzo et al., 2019), or by performing unpaired two-tailed Welch's t-test, or the Mann-Whitney test, the latter two of which were performed using GraphPad Prism. These latter tests were selected as follows: the unpaired two-tailed Welch's t-test was used when the datasets in question were both determined to be normal (by the D'Agostino and Pearson test for normality; $P > 0.05$); in the case where only one (or neither) of the datasets were determined to be normal ($P < 0.05$), the Mann-Whitney test was used.

Supplementary Materials

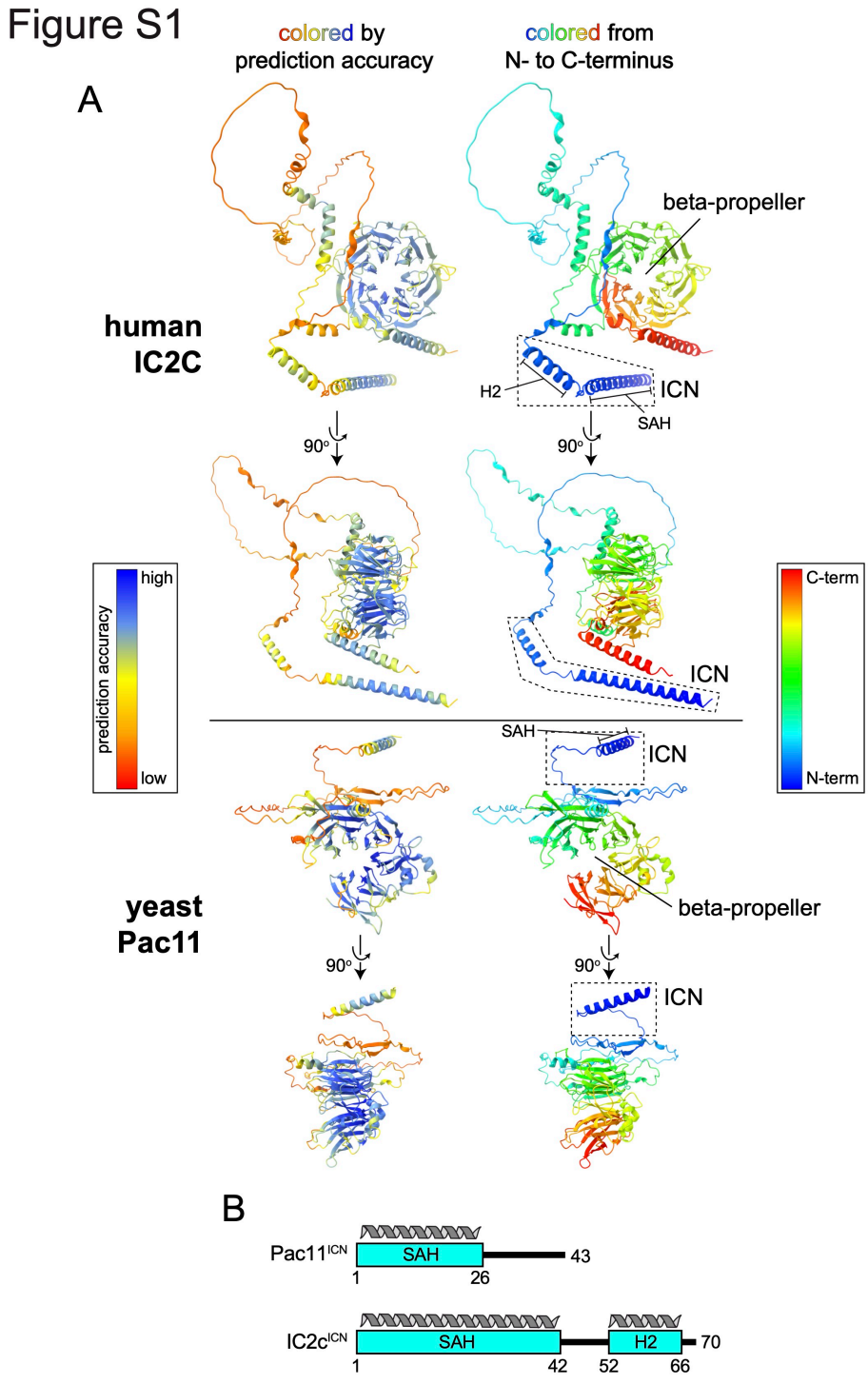

Figure S1. AlphaFold2-generated models of dynein intermediate chains from human and yeast. A AF2 Models are colored according to prediction accuracy (left) or from N- to C-terminus (right). **B** Schematic of yeast and human intermediate chain N-termini deleted in this study.

Figure S2

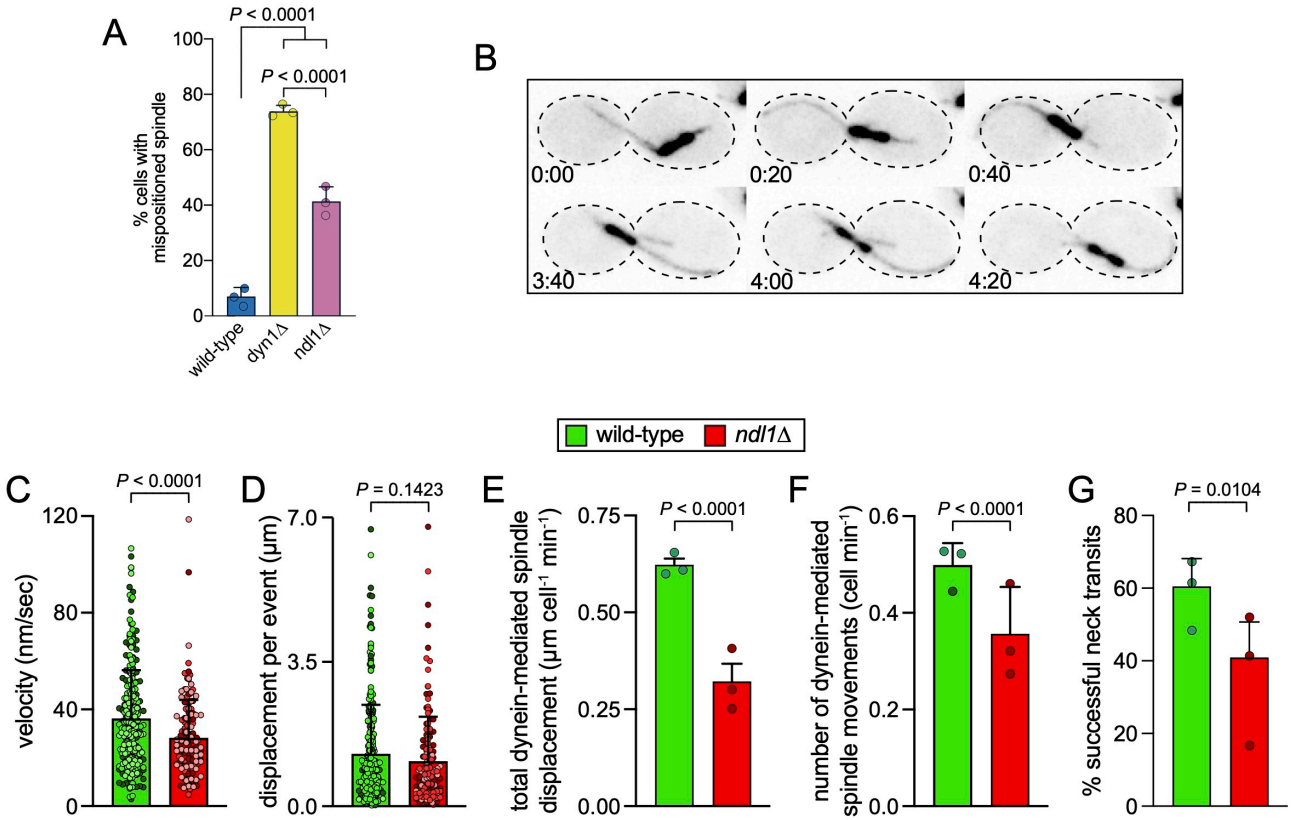

Figure S2. Quantitative assessment of Ndl1's role in dynein *in vivo* function. A Plot (mean ± SD, along with values from individual replicates) depicting fractions of cells exhibiting mispositioned anaphase spindles (n = 53/56/49 WT cells, 38/56/61 *dyn1Δ* cells, and 62/61/55 *ndl1Δ* cells, all from 3 independent replicates). *P* values were generated by calculating Z scores. **B** Representative time-lapse inverse fluorescence images of a hydroxyurea (HU)-arrested *kar9Δ* cell (*KAR9* was deleted to more reliably score dynein-dependent spindle movements) exhibiting typical dynein-mediated spindle movements. **C - G** Plots of indicated parameters for spindle dynamics in *kar9Δ NDL1* and *kar9Δ ndl1Δ* strains. Briefly, the mitotic spindles were tracked in 3-dimensions using a custom written Matlab code (Ecklund et al., 2023; Marzo et al., 2019). Dynein-mediated spindle movements were manually selected from the tracking data, from which velocity **C**, displacement (**D**, per event; or, **E**, per minute), and the number of dynein-mediated spindle movements per minute **F** were obtained. The fraction of successful neck transits (G; successful attempts divided by total attempts) were manually scored. Each bar represents the mean ± SD (shown along with the means from each independent replicate; n = 20/20/20 and 19/17/20 HU-arrested WT and *ndl1Δ* cells, respectively, from 3 independent replicates). For panels **C - G**, *P* values were calculated using a Mann-Whitney test or an unpaired Welch's t-test.

Figure S3

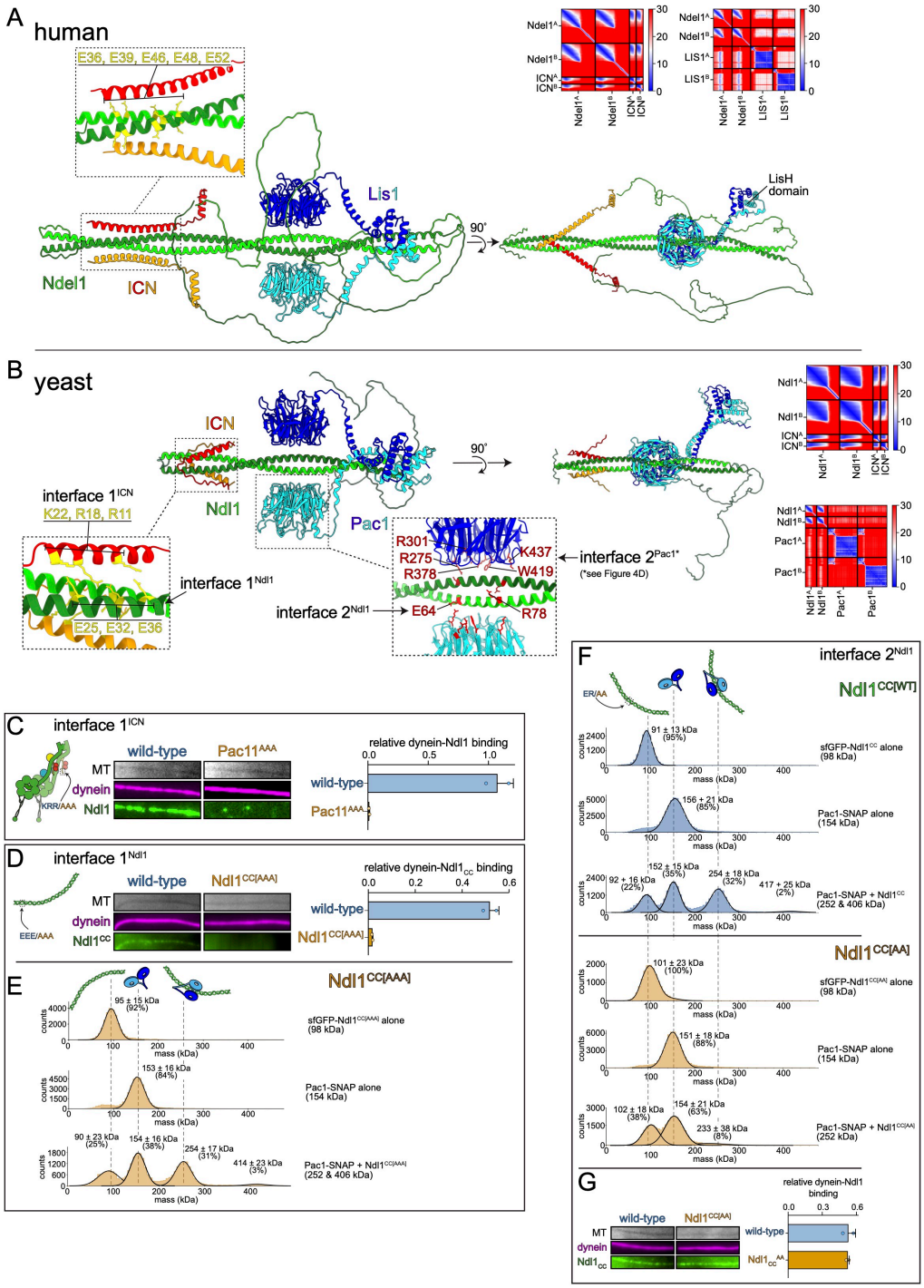

Figure S3. AlphaFold2-Multimer predictions of Ndel1/Ndl1-LIS1/Pac1-ICN complex structures, and validation thereof. A Model of Ndel1-LIS1-ICN complex (dimers of each) along with predicted alignment error (PAE) plots. Note that models of Ndel1-LIS1 and Ndel1-ICN were generated independently, and assembled into a co-complex using ChimeraX. Inset shows residues on Ndel1 previously shown to be important for interaction with dynein (Wang and Zheng, 2011). **B** Model of Ndl1-Pac1-ICN complex (dimers of each) along with PAE plots. Note that models of Ndl1-Pac1 and Ndl1-ICN were generated independently and assembled into a co-complex using ChimeraX. Insets show residues on Ndl1, Pac1 and ICN predicted by AF2 models that would be important for contacts at interface 1 (ICN-Ndl1) and interface 2 (Pac1-Ndl1). **C and D** Representative images from TIRFM binding assay and plots (mean ± SD, along with mean values from independent replicates) depicting the effect of mutating interface 1 on either Pac11 (R11A, R18A, K22A; in the context of the full-length dynein complex purified from yeast) or Ndl1^{CC} (E25A, E32A, E36A) on the Ndl1-dynein interaction (n = 20 MTs for each data point from 2 independent replicates). **E** Mass photometric analysis of individual proteins, or mixtures of proteins, as indicated. Note that Ndl1$^{CC[AAA]}$, which doesn't bind to dynein, is competent for interaction with Pac1 (apparent from 254 kDa species). **F** Mass photometric analysis of individual proteins, or mixtures of proteins, as indicated, depicting the effect of mutating interface 2 on Ndl1^{CC} (E64A, R78A) on its interaction with Pac1. Note that Ndl1$^{CC[AA]}$ cannot bind Pac1, as is apparent from lack of 254 kDa species. **G** Representative images from TIRFM binding assay and plot (mean ± SD, along with mean values from independent replicates) depicting the ability of Ndl1$^{CC[AA]}$ to interact with dynein (n = 20 MTs for each data point from 2 independent replicates).

Figure S4

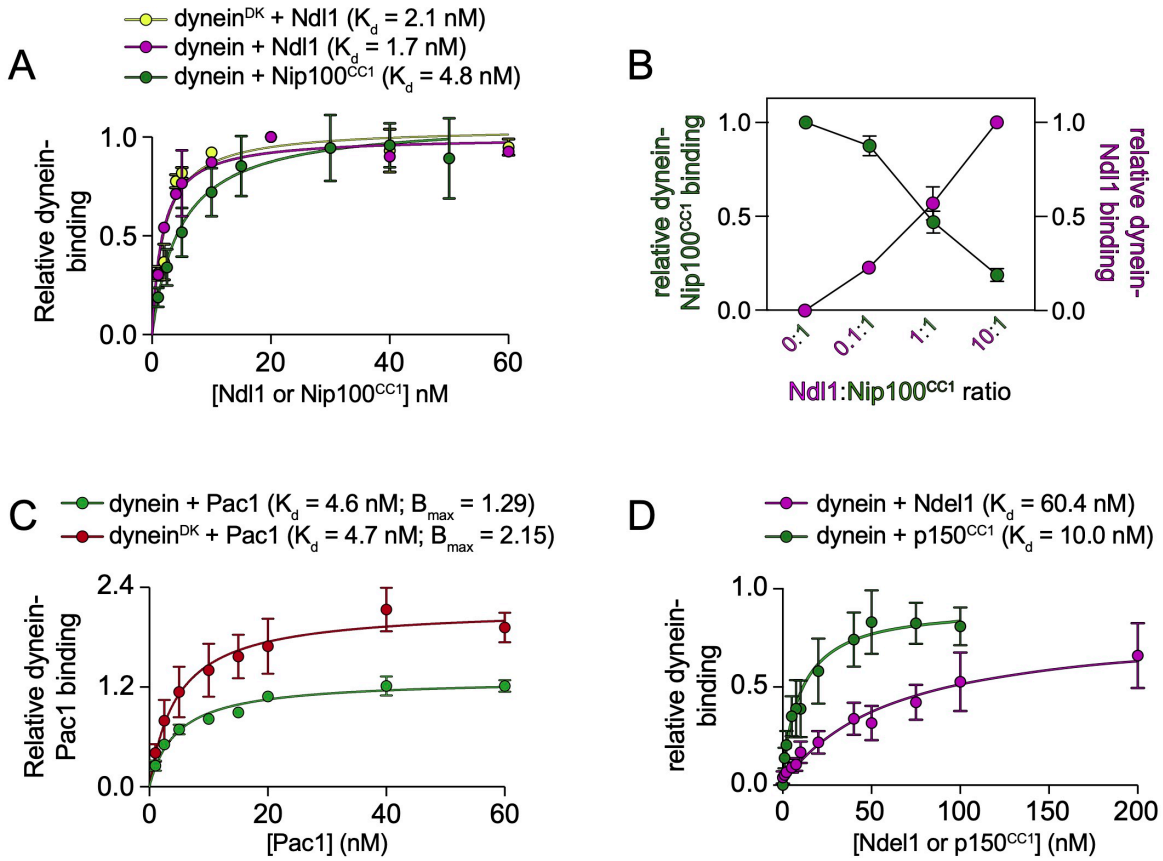

Figure S4. Relative binding affinities of dynein for p150^{CC1}/Nip100^{CC1} and Ndel1/Ndl1 . A Plot depicting relative dynein-Ndl1 (wild-type, or D2868K 'open' mutant, "dynein^{DK}") or dynein-Nip100^{CC1} binding, as determined by TIRFM-based assay. The full-length dynein complex (wild-type or dynein^{DK}, as indicated; both purified from yeast) was incubated with indicated concentrations of either Ndl1 or Nip100^{CC1}, and introduced into an imaging chamber with coverslip-immobilized microtubules. Relative binding at indicated concentrations of Ndl1 and Nip100^{CC1} was measured (determined from background corrected microtubule-localized intensities of Ndl1-SNAPf^{JFX554} divided by that of HALO^{JF503}-dynein, or eGFP-Nip100^{CC1} divided by that of HALO^{JFX549}-dynein), and then plotted and fitted to binding curves using Graphpad Prism. Each point represents the mean ± SD (n = 20 MTs for each data point from 2 independent replicates). **B** Plot depicting relative dynein-Ndl1 and dynein-Nip100^{CC1} binding (determined as in B) for indicated ratio of Ndl1:Nip100^{CC1}. For each datapoint, a fixed concentration of full-length dynein was incubated with a mixture of Ndl1 and Nip100^{CC1}, introduced into an imaging chamber with coverslip-immobilized microtubules, and immediately imaged. Each point represents the mean ± SD (n = 20 MTs for each data point from 2 independent replicates). **C** Plot depicting relative Pac1 binding by dynein (wild-type, or dynein^{DK}, as indicated; determined as in B) for indicated concentration of Pac1. Each point represents the mean ± SD (n = 20 MTs for each data point from 2 independent replicates). **D** Plot depicting relative dynein-Ndel1 or dynein-p150^{CC1} binding, as determined by TIRFM-based assay. The full-length human dynein complex was incubated with indicated concentrations of either Ndel1 or p150^{CC1}, and introduced into an imaging chamber with coverslip-immobilized microtubules. Relative binding was measured as above in panel A (n = 59/51, 61/53, 55/55, 52/51, 61/56, 61/57, 62/50, 81/57, 67/53, 76/55, 64/55, 64/55, 51/51 for Ndel1, 59/59, 56/60, 60/54, 61/58, 53/56, 90/71, 59/66, 90/64, 85/57, 54/59, 56/56 for p150^{CC1} from two independent replicates)